



Article

Mineralogy, Fluid Inclusions, and Oxygen Isotope Geochemistry Signature of Wolframite to Scheelite and Fe,Mn Chlorite Veins from the W, (Cu,Mo) Ore Deposit of Borralha, Portugal

Iuliu Bobos ^{1,*} , Carlos Marques de Sá ² and Fernando Noronha ¹ 
¹ ICTerra-Porto, Faculdade de Ciências, Universidade do Porto, 4168-007 Porto, Portugal; fmnoronh@fc.up.pt

² Grupo de Pesquisa em Recursos Minerais, Departamento de Geologia, Universidade Federal de Sergipe, Aracaju 49060-108, SE, Brazil; dingester@gmail.com

* Correspondence: ibobos@fc.up.pt

Abstract: Scheelitization of Mn-bearing wolframite, scheelite, quartz, and Fe,Mn-chlorite veins was identified in the W, (Cu,Mo) ore deposits of Borralha, by optical microscopy, electron-microprobe analysis, and stable isotope geochemistry. Fluid inclusions derived scheelite crystallization temperature was compared with the oxygen isotope temperature estimated. Scheelite was formed mainly during stage I from a low salinity aqueous-carbonic fluid dominated by CO₂, where the homogenization temperature (T_h) decreased from 380 °C to 200 °C (average of 284 °C). As temperature decreased further, the aqueous-carbonic fluid became dominated by CH₄ (Stage II; (average T_h = 262 °C)). The final stage III corresponds to lower temperature mineralizing aqueous fluid (average T_h = 218 °C). In addition, salinity gradually decreased from 4.8 wt.% to 1.12 wt.%. The $\delta^{18}\text{O}_{\text{Fluid}}$ values calculated for quartz-water and wolframite-water fractionation fall within the calculated magmatic water range. The $\Delta_{\text{quartz-scheelite}}$ fractionation occurred at about 350–400 °C. The $\Delta_{\text{chlorite-water}}$ fractionation factor calculated is about +0.05‰ for 330 °C, dropping to −0.68‰ and −1.26‰ at 380 °C and 450 °C, respectively. Estimated crystallizing temperatures based on semi-empirical chlorite geothermometers range from 373 °C to 458 °C and 435 °C to 519 °C. A narrower temperature range of 375 °C to 410 °C was estimated for Fe,Mn-chlorite crystallization.

Keywords: wolframite scheelitization; Fe,Mn-chlorite; H₂O-CO₂ (CH₄) fluid inclusion; stable isotope fractionation; chlorite geothermometry; Borralha; Portugal



Citation: Bobos, I.; de Sá, C.M.; Noronha, F. Mineralogy, Fluid Inclusions, and Oxygen Isotope Geochemistry Signature of Wolframite to Scheelite and Fe,Mn Chlorite Veins from the W, (Cu,Mo) Ore Deposit of Borralha, Portugal.

Minerals **2022**, *12*, 24. <https://doi.org/10.3390/min12010024>

Academic Editors: Harald G. Dill and Jan Marten Huizenga

Received: 18 September 2021

Accepted: 21 December 2021

Published: 23 December 2021

Publisher's Note: MDPI stays neutral with regard to jurisdictional claims in published maps and institutional affiliations.



Copyright: © 2021 by the authors. Licensee MDPI, Basel, Switzerland. This article is an open access article distributed under the terms and conditions of the Creative Commons Attribution (CC BY) license (<https://creativecommons.org/licenses/by/4.0/>).

1. Introduction

Tungsten mineralization in magmatic-hydrothermal deposits occurs predominantly as wolframite ([Fe,Mn]WO₄) and scheelite (CaWO₄). Wolframite is the main dominated tungsten mineral in granite-related systems, whereas in skarn deposits, it is scheelite [1–4]. Given the variability of the geological context in which scheelite occurs in nature- scheelite-quartz vein mineralizations and greisen in granite [5–8], quartz-scheelite veins in metabasite [9], scheelite in orogenic gold [10], and skarn deposits [11], published scheelite fluid inclusions (FIs) are somewhat limited.

Scheelite related to quartz veins and greisen (e.g., Yangjiashan, China) include vapor- and liquid-rich FIs types with detectable CH₄, CO₂, and N₂, where the T_h ranges (mean values) from 230 °C to 250 °C and salinity (mean values) from 9.3 wt.% to 6.6 wt.% NaCl equiv. [12]. In addition, ore-forming fluids show intermediate to low temperatures that belong to the H₂O-NaCl ± CO₂ system in the disseminated scheelite associated with potassic feldspathization and silicification of porphyritic biotite granite from the Wuyi metallogenic belt (China) [13].

In the quartz-scheelite veins hosted in metabasites (e.g., Metagitsi area, Greece), the most abundant FIs consist of H₂O-CO₂ with highly variable CO₂ contents (20 ± 90 vol.%) and

salinity between 0.2 wt.% and 8.3 wt.% NaCl equiv., where the homogenization temperature of aqueous and gas-rich type inclusions has been estimated to about 220 ± 25 °C (mean values) [9]. Furthermore, scheelite has a distinctive trace elements composition from various deposit types and geological environments, being considered an indicator mineral for orogenic gold [14]. Microthermometric and Raman spectroscopic studies of FIs have documented low salinity aqueous-gaseous ($\text{H}_2\text{O}-\text{CO}_2-\text{CH}_4-\text{NaCl}$) ore fluids, where gold and scheelite precipitated in orogenic gold deposits from the Dharwar craton (South India) [15].

The FIs of scheelite crystallized during the cooler period of skarn development (e.g., Kara, Tasmania) consist of primary $\text{H}_2\text{O}-\text{CO}_2$ with moderate salinity (12.0 wt.% and 17.8 wt.% NaCl equiv.) and homogenization temperatures of 350–580 °C [16]. A similar thermal history and scheelite formation were observed for other W skarn deposits (e.g., CanTung Mine, Northwest Territories, Canada) [17,18]. Recently, scheelite-bearing albitite (no FI data are known) was identified in the Zhuxi (China) skarn tungstate deposit as a product of a silicate-poor, H_2O -rich melt that formed by melt-melt-liquid immiscibility in an extremely fractionated residual magma [19].

The scheelite occurrences mentioned above showed a connection with a magmatic-hydrothermal, metamorphic, or hydrothermal-meteoric fluid of low to moderate salinity, where homogenization temperatures ranged from 220 °C to 580 °C. Concerning the source and evolution of ore-forming fluids, the mechanisms and thermodynamic conditions of scheelite deposition have yet to be addressed [20,21]. In addition, in most related cases, scheelite was found associated with quartz veins, greisen, albitite, or secondary K-feldspar. Nevertheless, there are no published data available in the literature regarding the association of scheelite with chlorite.

Scheelite from the W, (Cu,Mo) ore deposit of Borralha is associated with wolframite, Fe,Mn-chlorite, and quartz, where Mn-bearing wolframite has been replaced by scheelite. The relationships “*chlorite vs. metal assemblages*” have been revisited and explored, aimed towards using chlorite as a “proxy” for detecting porphyry ore deposits [22] because the large variety of chlorite minerals can serve as a tool to determine the direction towards a mineralized area, to estimate the temperatures under which the ore processes took place [23,24], or to estimate the heat flux away from a magmatic-hydrothermal centre [25].

The stability of the Fe^{2+} end-member wolframite (ferberite) is much more sensitive to the high variation of f_{O_2} than the Mn^{2+} end-member wolframite (hübnerite) and the composition of ferberite might also be strongly affected by the oxidation state of the system [26]. The physicochemical parameters (e.g., temperature, $\text{Mn}^{2+}/\text{Fe}^{2+}$ ratio in the mineralizing solution) during wolframite crystallization influence the hübnerite vs. ferberite proportions of wolframite [27].

Furthermore, redox state exchange between Fe- and Mn-distributions in chlorite associated with wolframite and scheelite from the Borralha deposit showed that its composition is directly influenced by thermal gradients of the evolution of different stages within the magmatic-hydrothermal system [28], where the diversity of chlorite minerals associated with W-mineralization serves as an excellent indicator to identify mineralization areas and to estimate crystallization temperatures. Geothermometers have been developed for the Al-, Fe-, or Mg-rich chlorites and little is known about the specific chlorite systems, like Mn-rich chlorite, where a new question arises on Mn-redox, analogously to Fe-redox processes [29].

The application of empirical geothermometers to ore deposit research depends on complementary data regarding the mineralogical reaction mechanisms, estimation of P-V-T-X parameters of the ore-forming fluids or ones circulated through rocks, and the stable isotope geochemistry of neoformed minerals, helping to understand mineral history. Understanding the principles governing isotopic variations in nature is still limited due to the magnitude of isotopic fractionation that accompanies various geological processes and the diversity of fluids circulation mechanisms in the oceanic or continental crust, where geochemical parameters and the kinetic isotope effects accompanying a conversion of one mineral to another under a variety of conditions.

The main aim of this study is to characterize the mineralogy of scheelite + Fe,Mn-chlorite \pm wolframite scheelitized assemblages found in large crystalline Fe,Mn-chlorite masses in a W veins system, the chemistry of the fluids responsible for scheelite crystallization, where FIs data are coupled with Fe,Mn-chlorite geothermometry and the oxygen isotope geochemistry of wolframite, scheelite, quartz, and Fe,Mn-chlorite.

2. Geological Background

The Variscan orogeny is currently explained by an obduction-collision orogenic model [30–32], which distinguishes three main deformation phases (D1, D2, and D3) in northern Portugal [33,34]. The maximum crustal thickening was achieved by the end of the D1/D2 phases, whereas the D3 phase (intra-Westphalian age) corresponds to the final stages of the continental collision process. Most of the granitic intrusions and associated thermal metamorphic peaks are coeval with the D3 phase [30,35,36]. The syn- to late-orogenic magmatic activity generated voluminous granitoid batholiths often with contrasting compositions, where their emplacement was in most cases controlled by major Variscan structures.

The W, (Cu,Mo) deposit of Borralha is located in the Central Iberian Zone in northwestern part of the Iberian Peninsula of the (Figure 1a), where different syn-orogenic Variscan granites (e.g., two mica peraluminous, syn-D3, and biotite rich syn-D3) intruded Palaeozoic metasedimentary units. The ore deposits occur at the contact between metasedimentary formations (Silurian) and the syn-D3 porphyritic Borralha biotite granite (~315 Ma) and a syn-D3 two-mica granite (Figure 1b). The Borralha ore deposit was an important W deposit in Portugal explored for wolframite, scheelite, and argentiferous chalcopyrite during 1903–1985. W mineralization occurs in quartz veins and in the two breccia pipes known as Santa Helena and Venise [37]. The Santa Helena breccia (SHB) occurs in outcrops (Figure 1b), whereas the Venise breccia was found underground during mining works. Rock fragments of variable size, cemented with mineralized coarse-grained quartz aggregates, characterize both breccias. The underground works exploited vertical quartz veins (more than 45° dip, VV) and sub-horizontal veins or “flat veins” (<30° dip, FV). The main vertical veins mineralized with tungstates occur in the most central deposit part, located in the Santa Helena veins (e.g., Santo António, Santa Helena north, and Santa Helena south) and cross several lithologies including porphyroid biotite granite, tonalites, and schists. The dominant micaschist rocks to the east part are cross-cut by the main W veins subdivided into vertical veins sub-concordant with the schistosity, namely: The three north (3N) and three south (3S) veins. However, these lodes contain less mineralizations of tungstates and more sulphides (i.e., chalcopyrite). The ore mineral assemblages consist of tungstate (wolframite and scheelite), various sulphide minerals (chalcopyrite, pyrite, pyrrhotite, molybdenite, sphalerite, galena, bismuthinite, marcasite), native bismuth, and Pb-Bi-Ag sulphosalts. Fluid inclusion studies of quartz related to W mineralization have identified aqueous-carbonic fluids (300 °C < T < 400 °C and 50 MPa < P < 100 MPa) and aqueous fluids (250 °C < T < 300 °C and 30 MPa < P < 50 MPa) in sulphide mineralization [38,39].

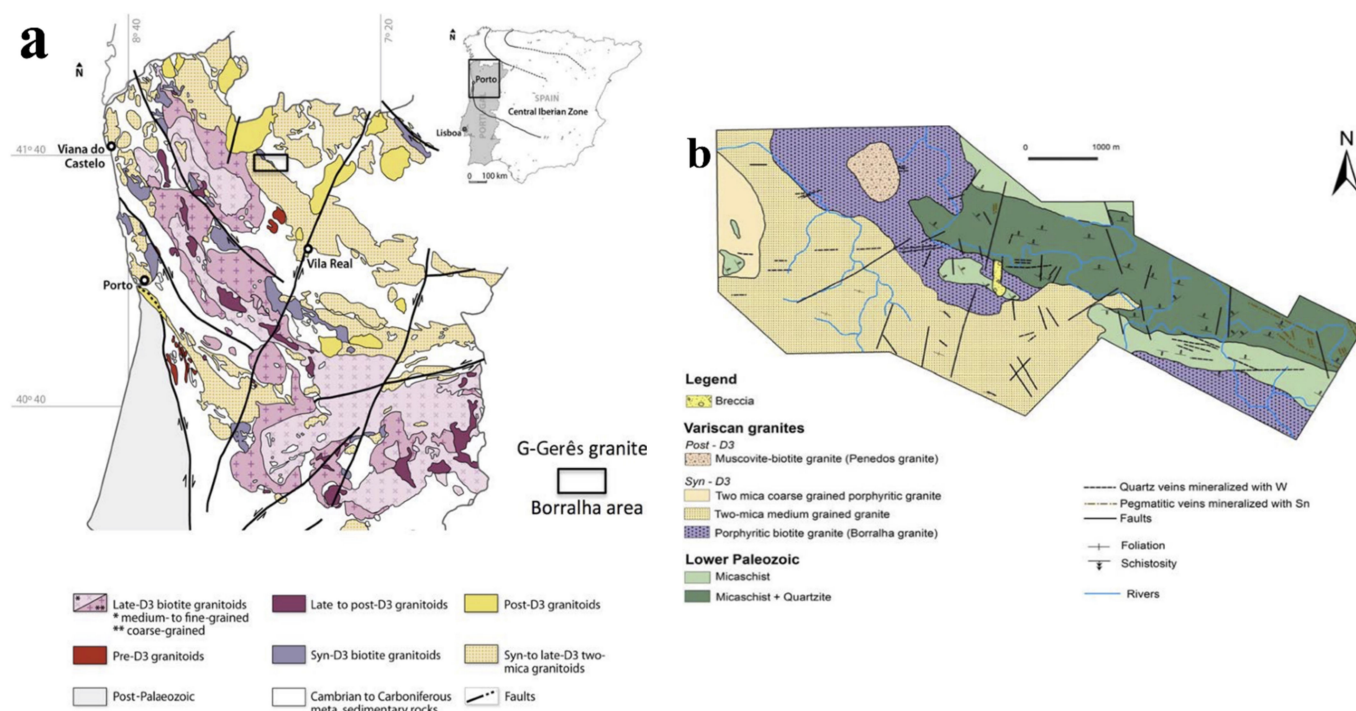


Figure 1. (a) Geological map of the northern part of Portugal and location of the W, (Cu,Mo) ore deposit of Borralha, Gerês Mountains [35]. (b) Geological map of the Borralha region [40]. (Both figures are reproduced from Bobos et al. [28] with permission of the Mineralogical Society of Great Britain and Ireland).

3. Materials and Methods

Sample collection. Wolframite to scheelite alteration and scheelite samples (SHS and 3N “vertical veins”) with crystal sizes of a few centimeters associated with Fe,Mn-chlorite in large crystalline masses collected from the Santa Helena veins (SHS) and northern gallery (3N) from the exploitation level (−60 m underground) of the Borralha ore deposit were selected for mineralogy, FI, and oxygen isotope geochemistry analyses.

Optical microscopy. The petrography of gangue and ore minerals was conducted by optical microscopy (transmitted and reflected light) using a Nikon microscope ECLIPSE model E400POL (Minato, Tokyo, Japan), coupled with an AxioCam camera ZEISS model MRc, connected to a computer with an AxioVision imaging software (SE64 Rel.4.9).

Electron microprobe analysis. Mineral compositions were obtained with an electron probe micro-analyzer (EPMA) Jeol Hyperprobe JXA-8500F (Tokyo, Japan) operated at a 15 kV accelerating voltage and with a 10 nA beam current in the case of silicates; the operation mode for the tungstates involves 20 kV and 20 nA, with counting times of 10 s on the element peaks and 5 s on the background position. The major elements of the minerals were determined using detection limits that were acceptably (σ) above the mean background of 0.02 wt.% for most sulphides and silicates with mean counting times of 80 s. The standards used for the silicates were: Albite (NaK α), orthoclase (AlK α , SiK α , KK α), apatite (CaK α , PK α), MgO (MgK α), MnTiO₃ (MnK α), TiO₂ (TiK α), and FeO (FeK α); for W minerals: Cassiterite (Sn K α), pure Ta (La), Mo (La), Ni (K α), Co (K α), Cu (K α), Ag (La), and Au (Ma) metals, SrBaNbO₄O₁₂ (Nb La), scheelite (WL α), Sc₂O₃ (Sc La), UO₂ (U M β), ThO₂ (Th M β), galena (Pb M α), LaP₅O₁₄ (La La), CeP₅O₁₄ (Ce La), YAg (Y La), Cd (La), Sb₂S₃ (SbLa), AsGa (As La), and Bi₂Se₃ (BiM α). The calculation of the structural formula was based on four oxygens for tungstate minerals and 14 oxygens for chlorite.

Fluid inclusion microthermometry. Four bi-polished plate thin sections (two from SHS and the other two from 3N “vertical veins”) were prepared and studied. Fluid petrography was performed on four scheelite (SHS1, SHS2, 3N1, and 3N2) bi-polished slide samples,

where about 50 FIs were observed per bi-polished sample plate. The petrographic study was carried out by transmission microscopy, using a Leica DM/LSP microscope (Wetzlar, Germany) equipped with objectives up to $50\times$ and a computer-controlled ICC50HD imaging system using the LAS EZ4 W software. The classification of FIs was performed according to the genetic criteria of Roedder [41], where the petrographic concepts of generations of FIs and fluid phase petrography were exposed by Van den Kerkhof and Hein [42], using Shepperd's et al. [43] abacuses. Microthermometric analyses were carried out using an Olympus microscope (Tokyo, Japan) with a maximum objective lens of $80\times$ and a $12\times$, equipped with a Chaixmeca stage [44] for cryometry, and a Linkam TH600 stage, coupled to a NIKON POL-Optiphot microscope, for heating. The calibration of the equipment was done regularly using a set of SynFlinch standards. The estimated accuracy was $-0.1\text{ }^{\circ}\text{C}$ for the Chaixmeca stage and $1\text{ }^{\circ}\text{C}$ in the Linkam stage. The salinity of the fluids was calculated with the help of the software developed by Bakker [45].

Raman spectroscopy. The study was conducted with a LabRam Dilor-JobinYvon-Spex (Lille, France) equipped with a He-Ne 632.8 nm laser source, coupled to an Olympus microscope with a $100\times$ objective. The spectral decomposition of the bands and Raman parameters was carried out with Dilor LabSpec-JobinYvon-Spex Raman software (version 1.1). Raman spectrometry analysis of aqueous-carbonic inclusions allowed the estimation of the bulk composition and density of the fluids using the methods and equations of Touret [46] and Ramboz et al. [47]. The calibration and other technical details are described in Prieto et al. [48].

Oxygen isotopes. The scheelite, quartz, and chlorite samples were selected for oxygen isotope analysis carried out at the Laboratory for Stable Isotopes at the University of Salamanca (Salamanca, Spain). A conventional procedure was used for the extraction of oxygen from scheelite, chlorite, and quartz with BrF_5 and the quantitative conversion to CO_2 prior to the analysis by stable-gas mass spectrometry [49]. The $\delta^{18}\text{O}$ values were reported in ‰ relative to the Vienna-Standard Mean Ocean Water (V-SMOW) and normalized to the NBS-30 reference (+5.17 per mil vs. V-SMOW) and NBS-28 (+9.34 per mil vs. V-SMOW). The accuracy of $\delta^{18}\text{O}$ measurements was $\pm 0.2\text{‰}$ (1σ). The following isotope fractionation equations were used in this work between minerals and water in the system: Wolframite- H_2O [50], scheelite- H_2O [51,52], chlorite- H_2O [53], and quartz- H_2O [54].

4. Results

4.1. Mineralogy

The selected samples (3N and SHS) are characterized by the following mineral assemblages: (a) 3N: Wolframite, scheelite, Fe,Mn-chlorite, quartz, and (b) SHS: Fe,Mn-chlorite, scheelite. Fe,Mn-chlorite is represented by the following samples used for EPMA: FMN1, FMN2, FMN3, FMN8, FMN9, and FMN12.

Wolframite scheelitization. The wolframite crystals have been partially or totally replaced by scheelite in the samples analyzed. A net contact may be observed between wolframite (white field) replaced by scheelite (grey) (Figure 2a, NII). Small scheelite crystals occur along fissures or fractures and cleavages in wolframite, where the replacement of wolframite by scheelite developed a shredded texture (Figure 2b, NII) until complete replacement. Wolframite scheelitization implies a later circulation of a rich alkaline fluid (Ca^{2+}) (Figure 2c, NII).

In addition, small inclusions of sulphide (pyrite or chalcopyrite) were identified along fractures in wolframite (Figure 2d, N+). EPMA data of wolframite show a mixed composition between ferberite (F) and hübnerite (H), where the Fe amount of 0.53 atoms per formula unit (apfu) is higher than Mn (0.43 apfu) (Table 1).

The hübnerite and ferberite ratio (H/F) calculated shows values from 46.25% to 46.7%. Small amounts of Nb_2O_5 (0.18%), Ta_2O_5 (0.01%), and SnO_2 (0.01%) were also measured. EPMA data of scheelite show traces of Fe, Mn and also Nb, Ta, Mo, and Sn (Table 1). X-ray element maps of wolframite replaced by scheelite show the Fe, Mn, Ca, and W distributions in wolframite and scheelite crystals (Figure 3).

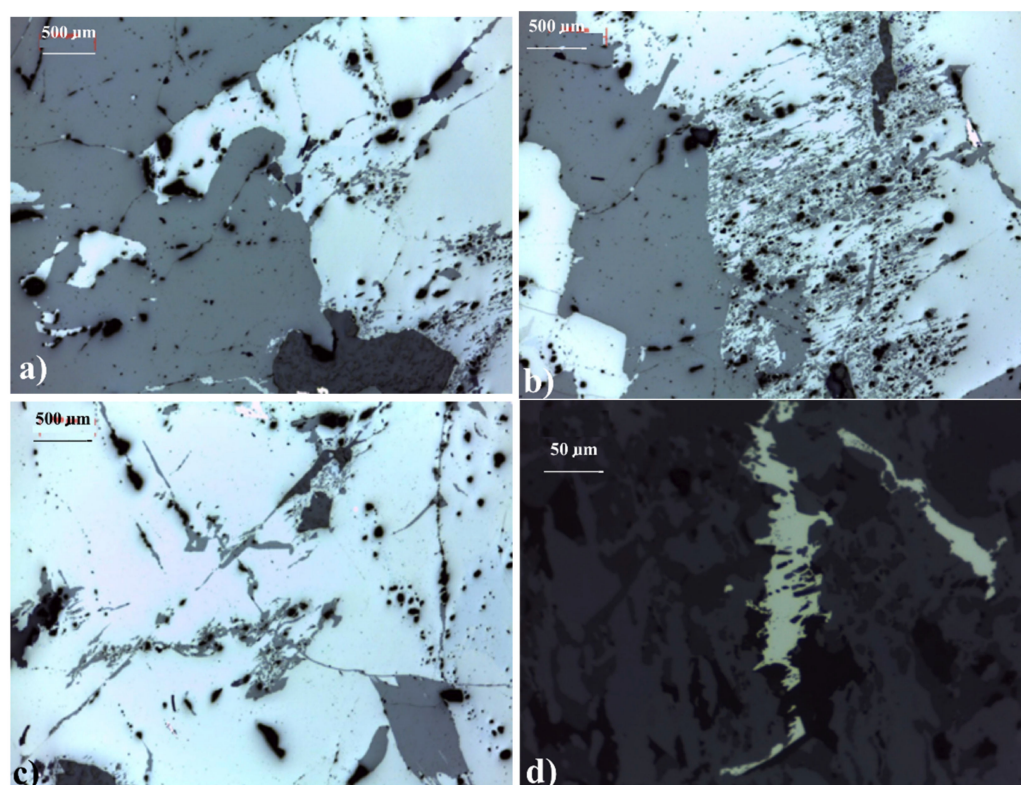


Figure 2. Photomicrographs showing textural relationships between wolframite and scheelite: (a) Wolframite (white field) replaced by scheelite (gray); (b,c) precipitation of scheelite crystals along to fissures or fractures of wolframite; and (d) inclusions of sulphide (pyrite) were identified along to fractures of wolframite.

Table 1. Electron microprobe data of wolframite and scheelite and calculus of structural formula based on four oxygens.

Oxides	10 Analyses Minimum	Fe,Mn-W Maximum	Fe,Mn-W Average	Sigma	14 Analyses Minimum	Scheelite Maximum	Scheelite Average	Sigma
WO ₃	75.12	76.35	75.94	1.23	79.29	80.85	80.34	2.14
FeO		12.88	12.51	0.7		0.07	0.02	0.0738
MnO		11.03	10.62	0.66		0.13	0.03	0.00994
CaO		0.01	0	0.0024		19.32	19.18	0.68
Sc ₂ O ₃		0.04	0.01	0.0274		0.02	0.01	0.02
Nb ₂ O ₅		0.26	0.18	0.13		0.2	0.04	0.164
SnO ₂		0.03	0.01	0.031		0.13	0.01	0.126
Ta ₂ O ₅		0.14	0.04	0.012		0.3	0.06	0.2951
TiO ₂		0	0	0		0.04	0.01	0.0172
V ₂ O ₃		0.04	0.02	0.02		0.08	0.02	0.0581
Bi ₂ O ₃		0.03	0.01	0.018		0.06	0.02	0.0453
MoO ₃						0.241	0.09	0.0321
Sb ₂ O ₅		0.05	0.02	0.02		0	0	0
Total		100.86	99.36			100.47	99.81	
W		0.99	1			0.99	1	

Table 1. Cont.

Oxides	10 Analyses Minimum	Fe,Mn-W Maximum	Fe,Mn-W Average	Sigma	14 Analyses Minimum	Scheelite Maximum	Scheelite Average	Sigma
Fe		0.54	0.53			0	0	
Mn		0.47	0.46			0	0	
Ca		0	0			0.98	0.99	
Sc		0	0			0	0	
Nb		0.01	0			0	0	
Sn		0	0			0	0	
Ta		0	0			0	0	
Ti		0	0			0	0	
V		0	0			0	0	
Bi		0	0			0	0	
Mo						0.02	0	
Sb		0	0			0	0	
Total		2.007	1.99			1.994	1.994	

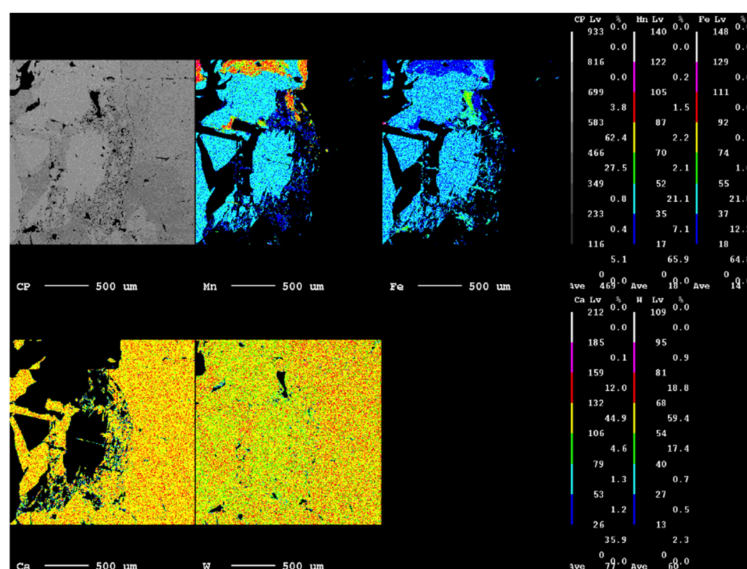


Figure 3. X-ray maps of Fe, Mn, and Ca distribution during wolframite scheelitization.

Scheelite. Scheelite (CaWO_4) aggregates adjacent to wolframite or Fe,Mn-chlorite were identified. The size of the scheelite aggregates reaches from $1 \text{ to } 1.5 \times 0.5 \text{ to } 0.75 \text{ cm}^2$. The color is orange to yellow-brown and fluoresces with a blue-white color, indicating low MoO_3 content (average $<0.09\%$). Traces of Sn, Pb, Bi, and Mo were measured in scheelite by EPMA (Table 1).

The average chemical composition of the scheelite associated with Fe,Mn-chlorite corresponds to $\text{W}_{1.00}\text{Ca}_{0.99}\text{O}_4$. The X-ray element maps show the W and Ca distributions in scheelite (Figure 4). Scheelite has a structure with tetrahedral $[\text{WO}_4]^{2-}$ and irregular dodecahedral $[\text{CaO}_8]^{14-}$ groups, where the hexavalent Mo can substitute for W, forming a complete solid solution series extending up to powellite (CaMoO_4) [55].

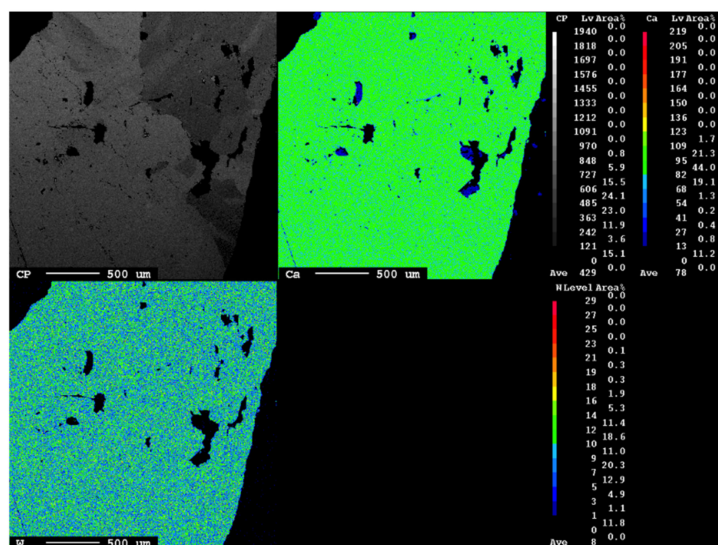


Figure 4. X-ray maps of W and Ca distribution in scheelite (reproduced from Bobos et al. [28] with permission of the Mineralogical Society of Great Britain and Ireland).

Fe,Mn-chlorite. Fe,Mn-chlorite aggregates observed in transmitted light under the microscope can be well identified by their green color pleochroism, varying from pale green for some massive aggregates to a dark pleochroism, a basal cleavage, and anomalous birefringence in cross-polarized light.

A strong pleochroism in green colors with an atypical dark orange interference color was observed (Figure 5), which is in accordance with the octahedral occupancy of heavy atoms (e.g., Mn^{2+}) [56] and the $\text{Fe} + \text{Mn}/\text{Fe} + \text{Mn} + \text{Mg}$ ratio [57]. The elongation sign is opposite to the optical one and the optical plane is almost parallel to (010). The Fe,Mn-chlorite aggregates are radial with a radius size ranging from 500 μm to 1000 μm .

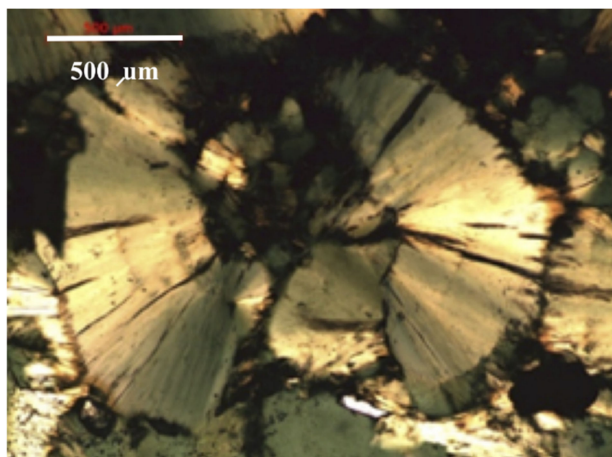


Figure 5. Photomicrograph showing radial aggregates of Fe,Mn-chlorite (NX).

The crystal chemistry of Fe,Mn-chlorite (Table 2) studied by EPMA shows an average crystal chemical composition (140 points analysed) corresponding to: $(\text{Al}_{1.385}\text{Fe}_{3.76}\text{Mn}_{0.59}\text{Mg}_{0.24}\text{Ca}_{0.01})_{5.99}(\text{Si}_{2.625}\text{Al}_{1.375})_4\text{O}_{10}(\text{OH})_8$. There is no tetrahedral substitution [$\text{Si} \leftrightarrow \text{Al(IV)}$], confirmed also by the calculated vacancy site (0.005) [58,59]. The R^{2+} exchanges (Mn^{2+} for Fe^{2+}) are evidenced in the octahedral sheet, also confirmed by the vacancy site calculated after Inoue et al. [59]. Small amounts of Zn^{2+} , Ca^{2+} , Na^+ , and K^+ were identified in Fe,Mn-chlorite. The ratio of $\text{Fe}/(\text{Fe} + \text{Mg})$ shows values from 0.92 to 0.94, whereas the $\text{Mg}/(\text{Mg} + \text{Fe})$ ratio is about 0.06. We also calculated the vacancy sites $(\text{Al}^{\text{VI}} - \text{Al}^{\text{IV}} - \text{Na} - \text{K})/2$ [58], $(\text{Al}^{\text{VI}} - \text{Al}^{\text{IV}})/2$ [59], and $6 - (\text{Fe}^{2+} + \text{Fe}^{3+} - \text{Mg} + \text{Al}^{\text{VI}})$ [60] (see Table 2).

Table 2. Electron microprobe data of Fe,Mn-chlorite and calculus of structural formula based on 14 oxygens ($\text{Fe}^{2+}/\text{Fe}^{3+}$ and OH calculated assuming full site occupancy).

Oxides	FMN 1 N = 31	FMN2 N = 29	FMN 3 N = 19	FMN 12 N = 22	FMN 8 N = 34	FMN 9 N = 11	Averages 146 Analyses
SiO ₂	23.18	22.7	23.2	23.11	23.73	22.46	22.82
TiO ₂	0.08	0	0.02	0.01	0.04	0.04	0.06
Al ₂ O ₃	19.88	19.95	19.82	19.82	20.14	20.86	20.37
FeO	39.52	39.86	39.53	39.13	39.55	38.59	39.055
MnO	6.23	5.03	5.82	6.21	5.28	5.81	6.02
MgO	1.87	1.44	1.88	1.67	1.75	1.01	1.44
CaO	0.04	0.01	0.03	0.05	0.05	0.06	0.05
Na ₂ O	0.03	0.03	0	0.01	0	0.01	0.02
K ₂ O	0.01	0	0	0	0	0.01	0.01
Total corrected by Cl + F	90.84	89.02	90.3	90.02	90.54	88.85	89.845
Si	2.64	2.64	2.66	2.66	2.69	2.61	2.62
Al IV	1.36	1.36	1.34	1.34	1.31	1.39	1.37
Total T site	4	4	4	4	4	4	4
Al VI	1.31	1.37	1.33	1.34	1.39	1.46	1.385
Ti	0.01	0	0	0	0	0	0.005
Fe ²⁺	3.77	3.87	3.78	3.76	3.75	3.75	3.76
Mn	0.6	0.5	0.56	0.6	0.51	0.57	0.585
Mg	0.32	0.25	0.32	0.29	0.3	0.17	0.245
Ca	0	0	0	0.01	0.01	0.01	0.005
Na	0.01	0.01	0	0	0	0	0.005
K	0	0	0	0	0	0	0
Total O site	6.02	6	6.01	6	5.96	5.97	5.995
Total Cations	10.02	10	10.01	10	9.96	9.97	9.995
OH [−]	8	8	8	8	8	8	8
Mg/(Fe + Mg)	0.08	0.06	0.08	0.07	0.07	0.04	0.06
Wt% H ₂ O calculated	10.52	10.32	10.48	10.43	10.57	10.33	10.425
Total Wt% (plus H ₂ O)	101.36	99.34	100.78	100.45	101.11	99.18	100.27
Vacancies							
(Al ^{VI} -Al ^{IV})/2 [58]	−0.02	0	−0.01	0	0.04	0.03	0.005
(Al ^{VI} Al ^{IV} -Na-K)/2 [59]	−0.02	0	−0.01	0	0.04	0.03	0.005
Calculation with Fe ³⁺ estimated	0	0	0	0	0.08	0.06	0.02
Mg/(Fe ²⁺ + Mg)	0.08	0.06	0.08	0.07	0.07	0.04	0.06
Vacancies							
6-(Fe ₂ + Fe ³ + Mg + A ^{VI})/2 [60]	0.6	0.5	0.56	0.61	0.56	0.62	0.61
(Al ^{VI} -Al ^{IV} + Fe ³ -Na-K)/2 [59]	−0.02	0	−0.01	0	0.04	0.03	0.005

Compositionally, the Fe,Mn-chlorite falls in the middle field between daphnite to amesite (Figure 6) in the diagram of R^{2+} vs. Si^{4+} [61].

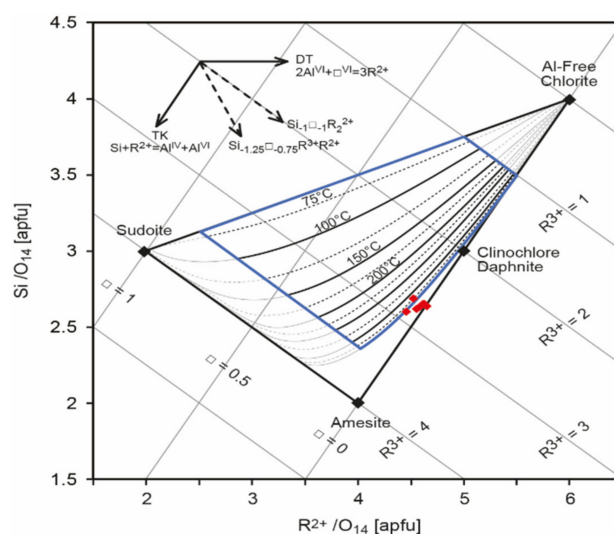


Figure 6. Chemical compositions of Fe,Mn-chlorite plotted in the R^{2+} -Si diagram [61]. Temperature estimation after Bourdelle [58].

The oxidation state of Fe,Mn-chlorite has previously been estimated [62], where the Fe^{3+} exhibited values between 0.00 and 0.08, with an average value of 0.02 for 145 spots analyzed.

4.2. Fluid Phase Petrography and Microthermometry

Petrography. The scheelite crystals exhibited fractures, making difficult the distinction between primary and secondary and pseudo-secondary inclusions.

The FIs occur in three preferred modes, namely: (i) In trails; (ii) isolated inclusions, and (iii) zonate ones (Figure 7; Table 3). Isolated inclusions are generally larger than 20 μm , whereas trails and zoning plane inclusions are smaller (average $\sim 10 \mu m$). The biggest measured FIs has a size about 160 μm with a negative crystal or oval shape, making the crystallographic form of the tetragonal crystal easy to identify. The FIs appear mostly dark due to internal reflections and occur in random clusters (primary inclusions) or in intergranular arrangements (pseudo-secondary inclusions).

Generally, the distinguished FIs are bi-phasic. Isolated tri-phasic primary FIs with a size exceeding 100 μm (sample SHS1), primary isolated FI, and intra-granular trails of pseudo-secondary FIs are shown in Figure 8a. Isolated FIs with a negative-crystal shape (sample SHS1), primary ones with a negative-crystal shape, and pseudo-secondary oval-shaped FIs in intra-granular trails are shown in Figure 8b. Large variations in the degree of fill (Φ_w) were also observed, especially in the 3N1-3N2 primary FIs and in both primary and pseudosecondary FIs of SHS1 and SHS2 (Table 3).

Freezing temperature, microthermometry, and salinity. The freezing temperature data include the first melting point, freezing depression, and melting of clathrate. Three different types of fluids in the FIs hosted by scheelite were identified: (i) Aqueous-carbonic fluids with CO_2 as the dominant carbonic phase, sometimes containing CH_4 and N_2 ; (ii) aqueous-carbonic fluids with CH_4 as the dominant carbonic phase, containing small amounts of CO_2 ; and (iii) aqueous fluids generally with a low to medium salinity. Aqueous-carbonic FIs with a dominant CH_4 phases (sample 3N1) are shown in Figure 9a,b; those with dominantly CO_2 phases (samples 3N2.1c, SHS1.3a, and SHS2.5b) are shown in Figure 9c,d.

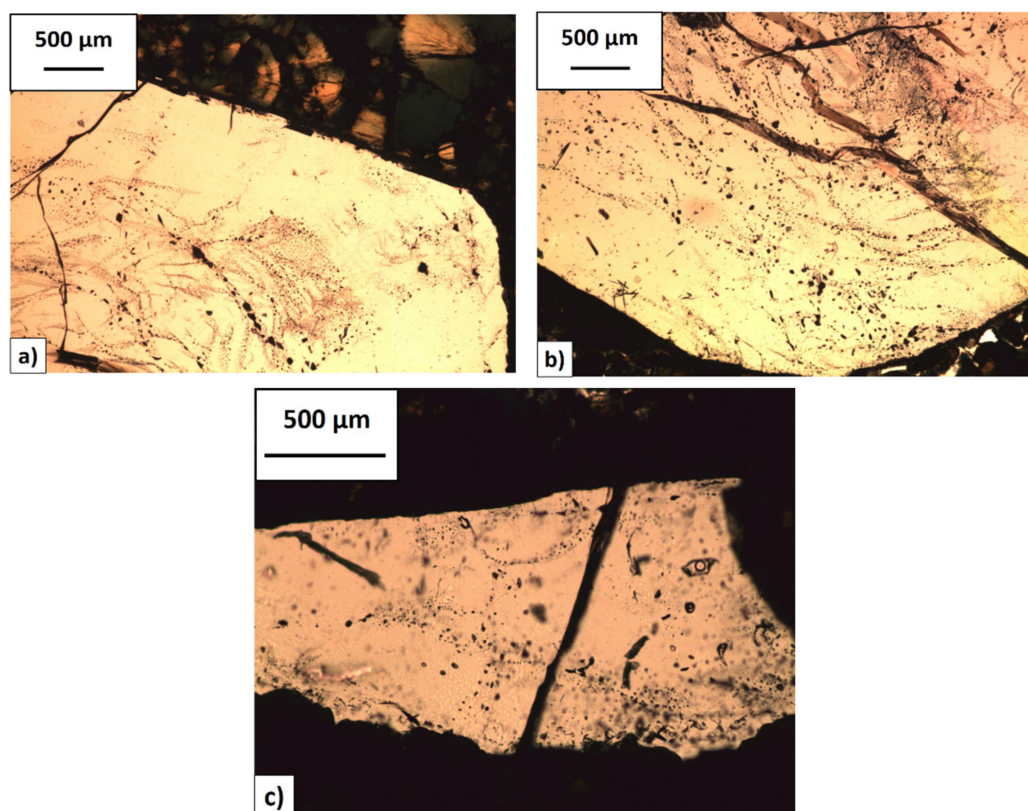


Figure 7. Photomicrographs showing: zonings and trails of fluid inclusions (a,b) and isolated fluid inclusions in sample SHS2 (c).

Table 3. Petrographic characteristics of fluid inclusions observed in scheelite. Degree of fill by liquid water is an approximate range. Size is generalized, the biggest fluid inclusions is 160 μm in the 3N1 sample (see photo Figure 8a). Total number of studied fluid inclusions was $n = 190$.

Samples	Type	Mode of Occurrences	Shape	Number of Phases	Size (μm)	Φ_w (%)
3N1 and 3N2	Primary	Isolated	Irregular or rectangular	2	>20	50–80
3N1 and 3N2	Pseudosecondary	Intragranular trails and clusters	Negative crystal, rectangular or oval	2	<30	70–80
SHS1 and SHS2	Primary	Isolated	Negative crystal and irregular	2	>20	50–70
SHS1 and SHS2	Pseudosecondary	Intragranular trails and clusters	Rectangular and negative crystal	2	<30	70–95

Microthermometric data of aqueous-carbonic fluids dominated by CO_2 are shown in Table 4. The T_{mice} of aqueous-carbonic FIs consisting mainly of CO_2 ranges from -7.2 $^{\circ}\text{C}$ to 0 $^{\circ}\text{C}$; T_{clat} from 0.2 $^{\circ}\text{C}$ to 11.5 $^{\circ}\text{C}$; T_h from 380 $^{\circ}\text{C}$ to 200 $^{\circ}\text{C}$; salinity from 3.5 wt.% to 5.5 wt.% NaCl equiv.; and 80 to 100 mol% XCO_2 . N_2 was only identified in six of the CO_2 -dominant aqueous-carbonic inclusions and always with $\text{XN}_2 < 8$ mol%. The T_{mice} of aqueous-carbonic FIs with dominant CH_4 ranges from -6.3 $^{\circ}\text{C}$ to 0 $^{\circ}\text{C}$; T_{clat} from 7 $^{\circ}\text{C}$ to 10.4 $^{\circ}\text{C}$; T_h from 323 $^{\circ}\text{C}$ to 220 $^{\circ}\text{C}$; salinity from 4.3 to 5.1 wt.% NaCl equiv.; and 100 mol% CH_4 (Table 4). The data for aqueous FIs are: T_{mice} from -5.7 $^{\circ}\text{C}$ to 0 $^{\circ}\text{C}$; T_h from 265 $^{\circ}\text{C}$ to 130 $^{\circ}\text{C}$; and salinity from 0 to 6.2 wt.% NaCl equiv. (Table 4).

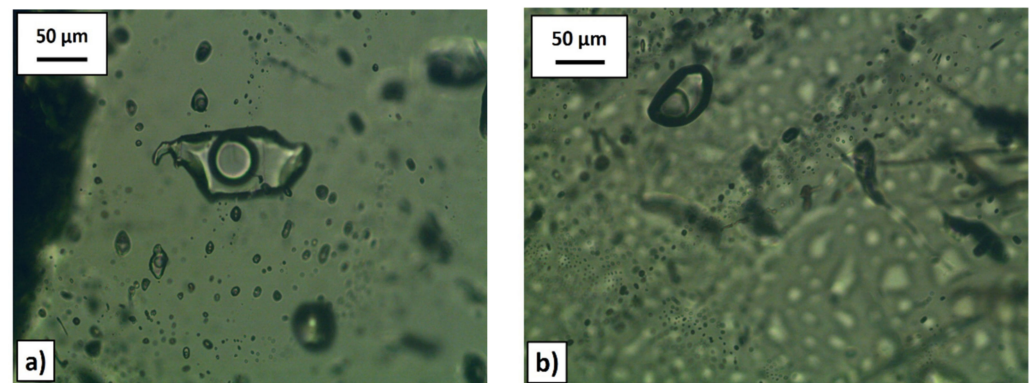


Figure 8. (a) Isolated bi-phasic primary fluid inclusions with a size of over 100 μm (sample SHS2, objective 5 \times). Other primary isolated fluid inclusions (back and front of the big isolated fluid inclusions) and intra-granular trails of pseudo-secondary fluid inclusions. (b) Isolated fluid inclusions in a negative-crystal shape (sample SHS1, objective 50 \times). Primary negative-crystal shape fluid inclusions and pseudo-secondary oval-shaped fluid inclusions in intra-granular trails are observed in the back side.

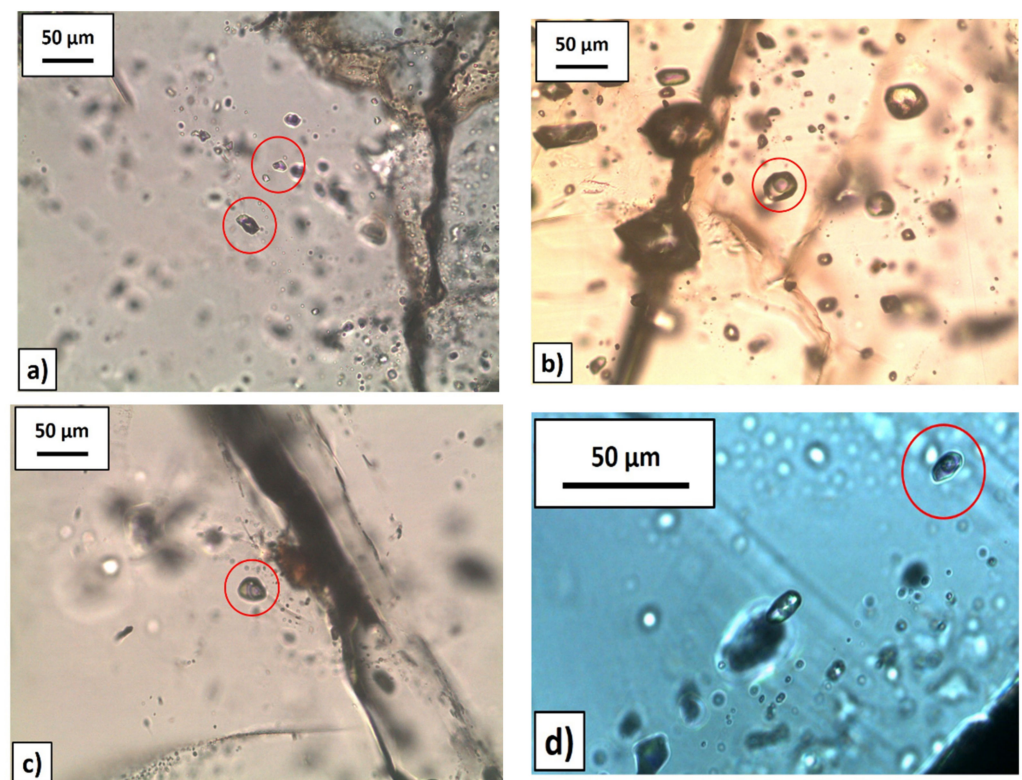


Figure 9. Aqueous-carbonic fluid inclusions: (a) Sample 3N1.6a and b predominantly CH_4 phase. (b) Sample 3N2.1c predominantly CO_2 phase. (c) Sample SHS1.3a predominantly CO_2 phase. (d) Sample SHS2.5b predominantly CO_2 phase.

Table 4. Microthermometric data for aqueous-carbonic fluid. AqCO₂—aqueous CO₂ FI; AqCH₄—aqueous CH₄ FI; N—number of analysis; Φ_w —degree of fill liquid water; T_e —eutectic temperature; T_{mice} —ice melting temperature; T_{clat} —clathrate melting temperature; T_h —homogenization temperature; Sal.—salinity in weight percent equivalents of NaCl; Xgas—amount of CO₂ or CH₄ in mol%; D—density in g/cc; Min-Max Av.—minimum, maximum, average.

Type		Φ_w (%)	T_e (°C)	T_{mice} (°C)	T_{clat} (°C)	T_h (°C)	Sal (wt.eq. NaCl)	Xgas (mol%)	D (g/cc)
AqCO ₂ (n = 79)	Min-max	50 to 80	−75.7 to −50	−7.2 to 0	0.2 to 11.5	200 to 380	3.5 to 5.5	80 to 100	0.55 to 1
	Av.	70	−59	−2.3	5.9	284	4.8	94.2	0.77
AqCH ₄ (n = 11)	Min-max	60 to 80	−68.7 to −52	−6.3 to 0	7 to 10.4	220 to 323	4.3 to 5.1	100	0.6 to 0.8
	Av.	75	−59	−2.5	9.4	262	4.7	100	0.8
Aqueous (n = 96)	Min-max	50 to 95	−67 to −23.1	−5 to 0		130 to 265	0 to 6.2		1 to 1.0
	Av.	82	−54.8	−0.75		218.5	1.18		1.01

Salinity (wt.% NaCl equiv.) measured for each type of fluid was plotted against T_h (°C) where three distinct evolution stages were distinguished (Figure 10). The first stage corresponds to the evolution of the aqueous-carbonic fluid with CO₂ dominating at high temperatures (<400 °C). The separation of carbonic phases shown in the T_h histogram occurred at about 330 °C through boiling.

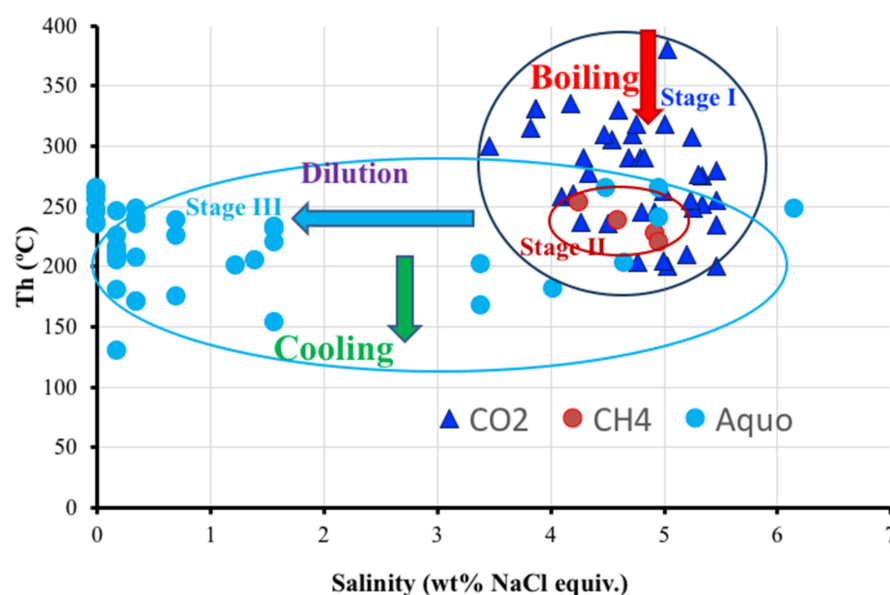


Figure 10. The diagram of salinity (wt.% NaCl eq.) vs. T_h (°C) corresponding to fluids identified in scheelite.

At this stage, the fluids lose their volatile components and start to precipitate their metals at the boiling point. Evidence for the boiling is also shown by the variations of liquid/vapor ratios observed in the FI and homogenization in liquid and vapor phase. The CH₄ and water were separated during decompression at temperatures below 300 °C and then mixed with an aqueous fluid of lower salinity. The T_h , T_{mice} , and salinity (wt.% NaCl equiv.) histograms corresponding to the whole set of FIs are shown in Figure 11.

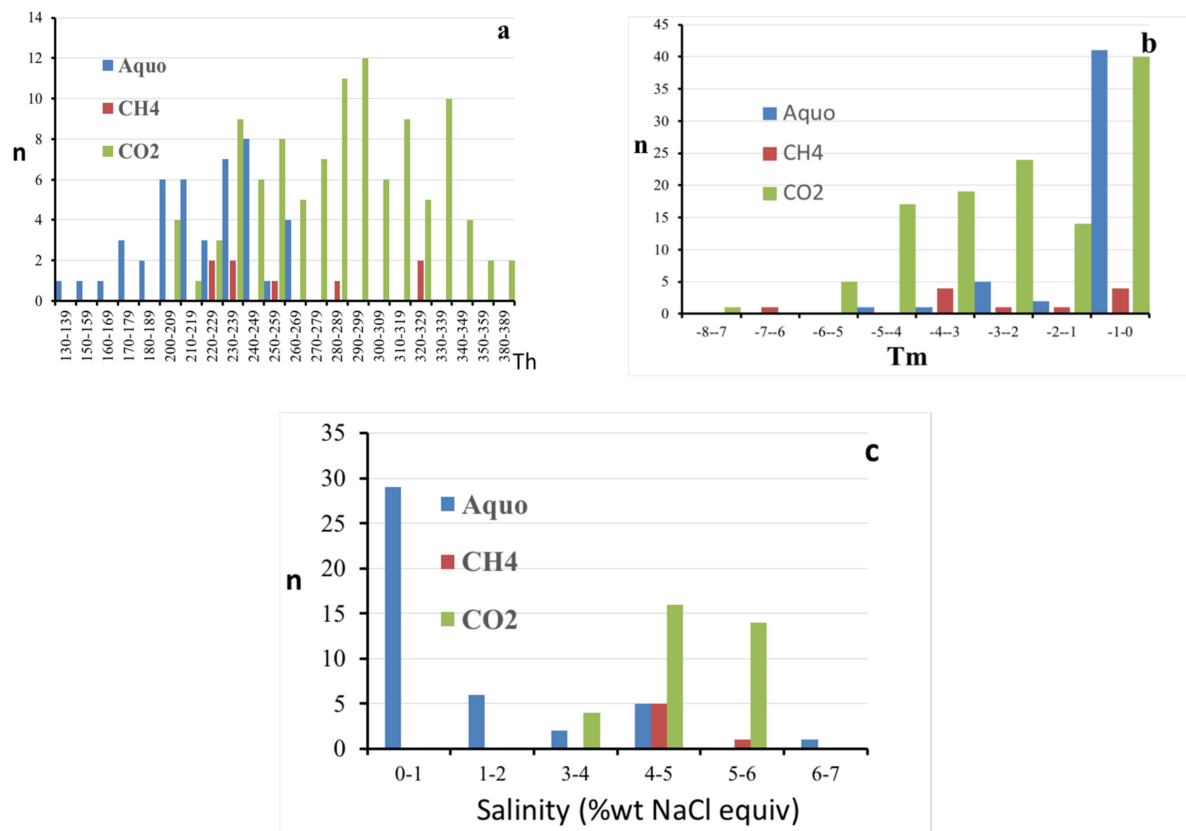


Figure 11. Histograms of T_h (a), T_m (b), and salinity of fluid inclusions (c) in scheelite from Borralha.

The T_{mi} and salinity histograms show that the hotter fluids were saltier (with about 5 wt.% NaCl equiv.) than the aqueous colder fluids which mixed at the end of the process. In addition, averages of the bulk compositions and densities of the FIs studied were calculated (see Table 4). No distinction between the primary and pseudosecondary inclusions could be established using the microthermometry of the fluid inclusion assemblages, but rather on the composition of the fluids. Raman spectrometry analyses were performed on representative aqueous-carbonic type (CO₂ or CH₄ dominant) FIs, where differences in the CO₂/CH₄ ratio were identified (Figure 12 and Table S1 in the Supplementary Materials).

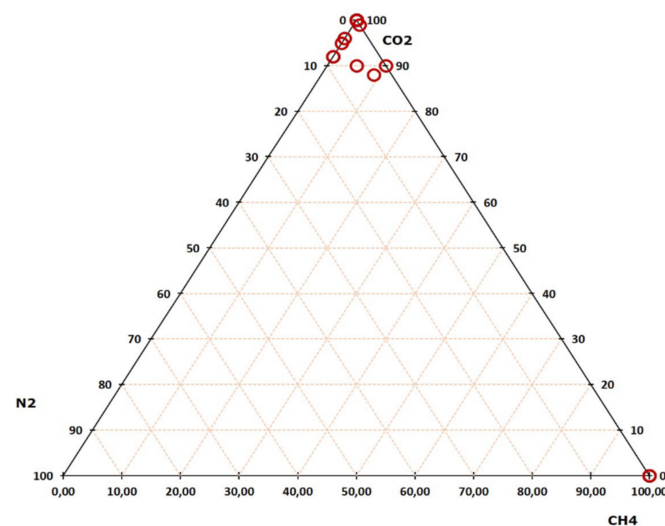


Figure 12. The ternary diagram of CO₂-CH₄-N₂.

4.3. Oxygen Isotope Analysis

Oxygen isotope measurements were obtained for quartz, wolframite, scheelite, and Fe,Mn-chlorite (Table 5), and previously published data on Fe,Mn chlorite [28] were re-analysed. The $\delta^{18}\text{O}$ isotope (V-SMOW) compositions of quartz (Q_{wf}) associated with wolframite shows a mean value of 12.6‰ (1 σ) and a mean value of 11.5‰ (1 σ) for the quartz join to scheelite.

Table 5. Oxygen isotope data of quartz, wolframite, scheelite and Fe,Mn-chlorite minerals.

Samples	Location	$\delta^{18}\text{O}$ (‰) $\mu\epsilon\alpha\sigma\nu\rho\epsilon\delta$	Quartz-Water Pair			Wolframite-Water Pair			Scheelite-Water Pair			Chlorite-Water Pair		
			300 °C	350 °C	400 °C	300 °C	350 °C	400 °C	300 °C	350 °C	400 °C	300 °C	350 °C	400 °C
Quartz (wf)	SHS 48 m	12.6	5.71	7.3	8.54	-	-	-	-	-	-	-	-	-
Quartz (sch)	3N	11.5	4.61	6.2	7.44	-	-	-	-	-	-	-	-	-
Wolframite	SHS-48 m	3.8	-	-	-	6.11	-	6.31	-	-	-	-	-	-
Scheelite	3N	2.8	-	-	-	-	-	-	4.44	5.09	5.6	-	-	-
Scheelite	3N	3	-	-	-	-	-	-	4.64	5.29	5.8	-	-	-
Scheelite	SHS 48 m	3.8	-	-	-	-	-	-	5.44	6.09	6.6	-	-	-
Fe,Mn-chlorite	3N	3.1	-	-	-	-	-	-	-	-	-	3.09	3.17	4.36
Fe,Mn-chlorite	SHS	3.2	-	-	-	-	-	-	-	-	-	3.15	3.27	4.46

The $\delta^{18}\text{O}_{\text{Fluid}}$ of the quartz-water pair ($10^3\ln\alpha_{\text{Quartz-water}} = 3.38 \times 10^6T^{-2} - 3.40$; [49]) yielded the following values for the precipitated quartz (Q_{wf}) associated with wolframite: +5.71‰ (1 σ) at 300 °C, +7.30‰ (1 σ) at 350 °C, and 8.54 (1 σ) at 400 °C. For the precipitated quartz (Q_{sch}) associated with scheelite yielded: +4.61‰ (1 σ) at 300 °C, +6.20‰ (1 σ) at 350 °C, and +7.44‰ (1 σ) at 400 °C (Table 5). The $\delta^{18}\text{O}$ (V-SMOW) measured for wolframite yielded a value of 3.8‰ (1 σ) (i.e., much lighter than quartz). The $\delta^{18}\text{O}_{\text{Fluid}}$ of the wolframite-water pair ($10^3\ln\alpha_{\text{Wf-water}} = 1.03 \times 10^6T^{-2} - 4.96$; and $10^3\ln\alpha_{\text{Wf-water}} = 0.21 \times 10^6T^{-2} - 2.91$ for temperature intervals between 250–370 °C and 370–420 °C [50]) yielded a value of 6.11‰ (1 σ) for an estimated temperature of 300 °C and 6.31‰ (1 σ) for 400 °C.

Combining the quartz-water fractionation equation [54] with the wolframite-water pair [50], the following oxygen isotope fractionation equations were proposed for the quartz-wolframite pair [63]: (i) 250–370 °C: $10^3\ln\alpha_{q-wf} = 2.35 \times 10^6T^{-2} + 1.56$ and (ii) 370–420 °C: $10^3\ln\alpha_{q-wf} = 3.17 \times 10^6T^{-2} - 0.49$. The quartz-wolframite oxygen isotope fractionation estimated for temperatures ranging from 300 °C to 400 °C yielded 9 and 7.11‰ (1 σ). The data plotted (not shown) in the $10^3\ln\alpha$ vs. T °C [63] fall between 300 °C and 400 °C.

The $\delta^{18}\text{O}$ isotope (V-SMOW) composition measured on scheelite yielded values of 2.8‰, 3‰, and 3.8‰ (1 σ). The $\delta^{18}\text{O}_{\text{Fluid}}$ of the scheelite-water pair ($10^3\ln\alpha_{\text{scheelite-water}} = 1.39 \times 10^6T^{-2} - 5.87$; [52]) yielded 4.44‰, 4.64‰, and 5.44‰ (1 σ) for 300 °C, 5.09‰, 5.29‰, and 6.09‰ (1 σ) for 350 °C, and 5.60‰, 5.80‰, and 6.60‰ (1 σ) for 400 °C (Table 5). The oxygen isotope fractionation in the quartz-scheelite and quartz-wolframite pairs is large, offering a much more sensitive geothermometer [64].

Combining the quartz-water fractionation equation [54] with the scheelite-water equation [52], the following fractionation equation was obtained for quartz-scheelite fractionation: $10^3\ln\alpha_{q-scheelite} = 1.99 \times 10^6T^{-2} + 2.47$. The $\Delta_{\text{quartz-scheelite}}$ calculated was 6.86‰ (1 σ) for a T °C of 400 °C and 7.54‰ (1 σ) for 350 °C. The $\Delta_{\text{quartz-scheelite}}$ values plotted in the diagram of $10^3\ln\alpha$ vs. T °C (not shown) intersected the quartz-scheelite fractionation curve at about 350–400 °C.

The $\delta^{18}\text{O}$ isotope (V-SMOW) signatures measured for Fe,Mn-chlorite yielded values of +3.1 and +3.2‰ \pm 1.2‰, where the $\delta^{18}\text{O}_{\text{Fluid}}$ calculated for the chlorite-water pair ($10^3\ln\alpha_{\text{chlorite-water}} = 1.56 \times 10^6T^{-2} - 4.70$; [53]) yielded +3.27‰ for a T °C of 350 °C, +4.46‰ for 400 °C (Table 5), and +4.92‰ for 450 °C. The $\Delta_{\text{chlorite-water}}$ fractionation factor calculated was about +0.05‰ for 330 °C and values of −0.68‰ and −1.26‰ corresponded to temperatures of 380 °C and 450 °C, respectively. After plotting the data in the $10^6 \times T^{-2}$

(°K) vs. $10^3 \ln \alpha_{\text{chlorite-water}}$ diagram (Figure 13) [65], an average crystallization temperature of 400 °C was obtained.

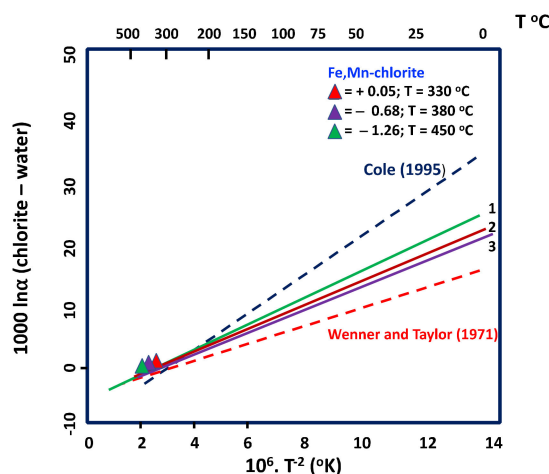


Figure 13. Estimation the oxygen isotope fractionation ratio between Fe,Mn-chlorite and water using the diagram of $10^6 \times T^{-2}$ (°K) vs. $10^3 \ln \alpha_{\text{chlorite-water}}$ [53,66].

4.4. Chlorite Geothermometry

Several chlorite thermometers based on empirical calibrations (linking T to Al^{IV} content) or semi-empirical models (linking T to the chlorite + quartz + water equilibrium constant) have been developed for Al-, Fe-, and Mg-rich chlorites over the last decade [58–60,67–69]. In a recent review on chlorite geothermometry, Bourdelle [29] noted that it could be worth applying these models for Mn-rich or Al-free chlorites to Mn-redox behavior, like Fe-redox.

In this study, 146 chemical analyses of Fe,Mn-chlorite (Table 2) were used for evaluating both empirical and semi-empirical models known in the literature. The average amount for FeO was about 39.05% and 6.05% for MnO, where the estimated Fe^{3+} was about 0.02 apfu. High contents of Fe [$\text{Fe}/(\text{Fe} + \text{Mg} + \text{Mn}) = 0.4\text{--}0.95$] and Mn [$\text{Mn}/(\text{Fe}^* + \text{Mg}) > 0.05$] in chlorite minerals are also diagnostic of chemical environments related to ore-forming processes [70]. The Fe,Mn-chlorite temperature values obtained using semi-empirical geothermometers [58–60,71] are shown in Table 6.

Table 6. Calculated temperatures using semi-empirical thermometry.

Samples Calculated Temperatures (°C)	FMN1	FMN2	FMN3	FMN12	FMN8	FMN9
Semi-Empirical Thermometry	T °C	T °C	T °C	T °C	T °C	T °C
Inoue et al. [60,71]. $\text{Fe}_{\text{Total}} = \text{FeO} + \text{Fe}_2\text{O}_3$. Quadratic equation thermometer (valid for <350°, may be <400 °C)	229	246	230	220	212	228
Inoue et al. [71]. $\text{Fe}_{\text{Total}} = \text{FeO}$ (valid for <350 °C, may be <400 °C)	197	210	197	190	183	196
Bourdelle et al. [58] $\text{Fe}_{\text{Total}} = \text{FeO}$. (Valid for <350 °C and <4 kb)	-	-	-	-	435	519
Lanari et al. [59]. Chl1: $\text{Fe}_{\text{Total}} = \text{FeO} + \text{Fe}_2\text{O}_3$ (valid between 100–500 °C)	-	-	-	-	718	984
Lanari et al. [59] Chl2: $\text{Fe}_{\text{Total}} = \text{FeO}$ (valid between 100–500 °C and 1–20 kbar)	-	-	-	-	373	458

The average calculated temperature of Fe,Mn-chlorite [59,70] was estimated at about 228 °C ($\text{Fe}_{\text{total}} = \text{FeO} + \text{Fe}_2\text{O}_3$) and 196 °C ($\text{Fe}_{\text{total}} = \text{FeO}$). The temperatures estimated for samples FMN 8 and FMN 9 were respectively about 435 °C and 519 °C ($\text{Fe}_{\text{total}} = \text{FeO}$) after Bourdelle [58] and 373 °C and 458 °C ($\text{Fe}_{\text{total}} = \text{FeO}$) after Lanari [59]. Here, the geothermometers of Bourdelle and Lanari [58,59] are not applicable (Table 7). The average temperature calculated for Fe,Mn-chlorite crystallization was about 373 °C, after Cathelineau [67], and 392 °C after Jowett [68]. The chemical composition of Fe,Mn-chlorite plotted in the Si^{4+} vs. R^{2+} diagram [61] falls into a field with temperatures ranging from 400 °C to 550 °C (Figure 6).

Table 7. Calculated temperatures using empirical thermometry *.

Samples Empirical Thermometry ($\text{Fe}_{\text{Total}} = \text{FeO}$)	FMN1 T °C	FMN2 T °C	FMN3 T °C	FMN12 T °C	FMN8 T °C	FMN9 T °C
Cathelineau [66]. (valid for <350 °C)	375	376	371	371	359	387
Jowett [67]. For Si < 3.3 apfu and Ca < 0.07 apfu. Fe/(Fe + Mg) < 0.6, and T° < 325 °C	393	395	389	389	377	406
Restrictions of each thermometer calibration (1 = Ok; 0 = not valid)						
Bourdelle et al. [58].	NOT APPLICABLE	NOT APPLICABLE	NOT APPLICABLE	NOT APPLICABLE	NOT APPLICABLE	NOT APPLICABLE
Uncertainty of 30 °C for T < 300 °C and 50–60 °C for T > 300 °C						
Na ₂ O + K ₂ O + CaO < 1? (wt.%)	1	1	1	1	1	1
Si (apfu) between 2 to 4 apfu	1	1	1	1	1	1
Vacancies > 0.05 apfu?	0	0	0	0	0	0
Lanari et al. [59].	NOT APPLICABLE	NOT APPLICABLE	NOT APPLICABLE	NOT APPLICABLE	NOT APPLICABLE	NOT APPLICABLE
Uncertainty of 50 °C.						
Si < 3 apfu	1	1	1	1	1	1
Na ₂ O + K ₂ O + CaO < 1? (wt.%)	1	1	1	1	1	1
Vacancies (Fe Total = FeOT) > 0.05 (for <0.05 = Thermometer Chl2 not applicable)	T° Chl2 should be not used	T° Chl2 should be not used	T° Chl2 should be not used	T° Chl2 should be not used	T° Chl2 should be not used	T° Chl2 should be not used
Inoue et al. [60,71].	Composition Valid	Composition Valid	Composition Valid	Composition Valid	Composition Valid	Composition Valid
Vacancies apfu < 1	1	1	1	1	1	1
Na ₂ O + K ₂ O + CaO < 0.5	1	1	1	1	1	1

* Thermometry calculations was carried out using the database of Verdecchia et al. [72].

5. Discussion

The successful application of chlorite minerals and stable isotope geothermometry to ore deposits requires several conditions to satisfy any pair of minerals: (i) Fractionation factors between them are well-calibrated and strongly temperature dependent; (ii) the mineral(s) species were in isotopic equilibrium at the time of deposition; and (iii) they have retained their isotopic composition since formation. Therefore, the sequence mineral pairs identified in the W, (Cu,Mo) ore deposit of Borralha satisfy all the requirements to evaluate the isotope geochemistry relationship between tungstates and neoformed silicates (quartz and Fe,Mn-chlorite) and empirical chlorite geothermometers, based also on FI microthermometry data.

5.1. Wolframite to Scheelite and Fe,Mn-Chlorite Crystallization

The scheelite samples collected are excellent samples due to their size, purity, and their genetic relationship with Mn-bearing wolframite and Fe,Mn-chlorite. Wolframite crystallized from fluids with slightly acidic to neutral pH, where WO_4^{2-} may be easily complexed with Fe^{2+} , Mn^{2+} , and Ca^{2+} . It should be noted that the stability of the Fe^{2+} end-member (ferberite) is much more sensitive to the high variations of f_{O_2} than the Mn^{2+}

end-member wolframite (hübnerite) since the composition of ferberite might be strongly affected by the oxidation state [26]. Only Mn-bearing wolframite is associated with the late evolving W mineralization, possibly triggered by an alkalinity rising in the fluid as a result of an increasing S activity and the availability of Ca^{2+} in the system, which is correlated with a late alkaline metasomatic reaction common in geochemical settings [73]. Several authors have suggested that Mn-rich wolframites precipitated at higher temperatures than Fe-rich wolframites [73–76]. Nevertheless, the H/F ratio used as a geothermometer [77] failed, because temperature is not the only factor controlling the composition of wolframite [27]. The H/F ratio can be used as an indicator of contrasting W deposition environments in perigranitic ore-forming systems, where hübnerite can be viewed as a relatively simple indicator of a strong magmatic control on W deposition [76]. The H/F ratio measured in wolframite samples from Borralha ranged from 46.25% to 46.70%, as a consequence of the high Mn/Fe ratio in the magmatic-hydrothermal fluid. By contrast, a H/F ratio < 40 and down to 0 indicates a W deposition environment where a significant non-magmatic contribution to the ore fluid and W deposition should be necessary [78].

Experimental studies on the stability of $\text{H}_4[\text{Si}(\text{W}_3\text{O}_{10})_4]2\text{H}_2\text{O}$ at high P-T conditions and variable pH in the presence of Ca^{2+} have confirmed the separation of silico-tungstic acid under the effect of solution neutralization [79], where $[\text{WO}_4]^{2-}$ is preferentially combined with Ca^{2+} to form scheelite, favoring the incorporation of the available Fe^{2+} and Mn^{2+} from wolframite and SiO_2 from the fluid into the chlorite structure. The CO_2 loss from the hydrothermal fluid during boiling caused pH changes from acidic to alkaline conditions [80–83], accompanying the wolframite dissolution and scheelite deposition in the presence of Ca^{2+} . Calcium for scheelite crystallization was supplied from the albitization and/or sericitization of plagioclase from granitic and pegmatite host rocks. Optical microscopy showed that the scheelitization of Mn-bearing wolframite occurred along fissures and fractures. This implies that high-pressure fluids are required to trigger fracture initiation and propagation, where the fluctuations of fluid pressure were recorded by FIs. Hence, Mn-bearing wolframite supported a dissolution process where $[\text{WO}_4]^{2-}$ separation served for scheelite crystallization, whereas Mn and Fe for chlorite. It is important to note that the term “metamorphic fluid” is used here to describe a fluid that was partially equilibrated with metamorphic rocks and this does not necessarily imply that the fluid components were produced from prograde metamorphic reactions.

5.2. Characterization of the Mineralizing Fluid

Previous FIs studies on scheelite from Borralha revealed two generations of FIs (primary and pseudosecondary) characterized by the presence of an aqueous, low salinity fluid [38]. The fluids entrapped in scheelites showed a complex history with different fluids and boiling during W precipitation, where boiling (immiscibility), mixing, cooling, and fluid-rock interactions (e.g., Ca^{2+} needed for scheelite precipitation) played an important role in the scheelite precipitation. The primary fluid stage was characterized by a complex aqueous-carbonic fluids of low salinity, indicating a typical metamorphic fluid. The CO_2 ubiquitous recorded in FIs from a variety of mineralized systems underwent boiling/unmixing presumably leading to ore deposition. Scheelite was mainly precipitated during the early stage from an aqueous-carbonic fluid with a CO_2 -dominated composition, where the T_h of the ore-forming fluids decreased from 380 °C to 200 °C.

Fluid boiling/immiscibility has two fundamental effects on the fate of metals. Indeed, it is known to induce the precipitation of some metals from the liquid phase owing to enhanced metal concentrations and to change the redox conditions and ligand contents in the residual liquid as a result of the removal of volatile components (H_2S , H_2 , HCl , and CO_2) into the vapor [81–83]. The partitioning of CO_2 and CH_4 into the vapor phase occurred through boiling, where both participated in redox reactions. The coexistence of vapor- and liquid-rich inclusions indicates fluid boiling/immiscibility. The boiling resulted in the separation of the aqueous-carbonic fluid with predominant CH_4 and mixing with an aqueous fluid of low salinity at about 330 °C, deduced from the histograms (Figure 8) and the diagram of salinity vs. T_h (Figure 9). The salinity (wt.% NaCl equiv.) vs. T_h

(°C) diagram shows two distinct fields corresponding to a magmatic-hydrothermal vs. metamorphic fluid (Stages I and II) and a hydrothermal-meteoric fluid (Stage III) (Figure 9).

Stage I occurred around the maximum T_h measured, corresponding to the beginning of separation between CO₂-CH₄ fluids during boiling (immiscibility). The L-rich FIs appeared to be in equilibrium with the CO₂-CH₄ inclusions (see Figures 10 and 11a), which is another indication of boiling. Boiling also increased oxygen fugacity, leading to the immiscibility of CH₄ where a disequilibrium isotopic fractionation occurred between CO₂ and CH₄ below 400 °C [83]. The process ended during the final of Stage II, when the aqueous saline FIs were generated. Changes in the aqueous-carbonic fluid composition were recognized as temperature decreased, where CH₄ became dominant (Stage II) and the T_h decreased (average of 262 °C). Stage III corresponded to the dilution of metamorphic fluids and cooling by the circulation of meteoric fluids. Exhaustion of deposition led to low salinity FIs. This stage corresponded to an aqueous fluid of lower temperature (average T_h = 218.5 °C). In addition, the salinity gradually decreased as temperature decreased (Figures 10 and 11c). The large dispersal of T_h values in the histogram and the reduced salinity observed for the aqueous inclusions was indicative of mixing.

Experimental studies have demonstrated that the solubility of scheelite decreases substantially with decreasing temperatures [73], where tungstate destabilization was influenced by the pH changes of the fluid [84]. This process removed CO₂ from the hydrothermal fluid, a component that can not only be a buffer fluid pH [73,85], but also favors W transport [86]. The trace amount of N₂ addition to the mineralizing fluids derived from the devolatilization of metasediments [87].

5.3. Oxygen Isotopes

The $\delta^{18}\text{O}_{\text{Fluid}}$ calculated for the quartz-water pair (sample Qwf) yielded values of + 5.7‰ at about 300 °C, + 7.30‰ at 350 °C, and + 8.54‰ at 400 °C, where the calculated values fall within the magmatic water field [88,89] from 5.5‰ to 10.0‰ [90–92]. In fact, from the isotopic point of view, quartz (Q_{wf}) and wolframite (+ 6.11 to + 6.31‰ at 300 and 400 °C, respectively) crystallized directly from a magmatic-hydrothermal fluid, which may represent primary magmatic water or water from any source whose isotopic composition is controlled by an exchange with a large volume of igneous rock. Nevertheless, the $\delta^{18}\text{O}_{\text{Fluid}}$ calculated for quartz (Q_{sch}) and scheelite yielded values from 5.55‰ to 6.6‰ for sample SHS, for temperatures ranging from 300 °C to 400 °C; for sample 3N values of 4.44‰ to 5.8‰ were obtained in the same temperature range. The samples analyzed suggest several scheelite generations crystallized from a magmatic-hydrothermal vs. metamorphic fluid (sample SHS) at temperatures below 400 °C, which were later diluted by a hydrothermal meteoric fluid (sample 3N). In fact, the differentiation between magmatic and metamorphic fluids in terms of $\delta^{18}\text{O}_{\text{Fluid}}$ is limited, creating difficult interpretations concerning the mixing of these two fluid phases. According with the FIs data, scheelite crystallization could be largely influenced by metamorphic fluids which equilibrated with the magmatic-hydrothermal fluid during the first wolframite crystallization. $\delta^{18}\text{O}_{\text{Fluid}}$ data support an input of hydrothermal-meteoric waters, confirming an exchange and re-equilibration with the primary fluid at elevated temperatures and low water/rock ratios. This assumption is supported by FIs data obtained from the studied scheelite samples, where an input of aqueous FIs after boiling was observed (Figure 10). Based on $\delta^{18}\text{O}$ data, it seems that Fe,Mn-chlorite crystallized in equilibrium with scheelite, but from a diluted hydrothermal-meteoric fluid contribution at a high temperature. The crystallization temperatures estimated from the $10^6 \times T^{-2}$ (°K) vs. $10^3 \ln \alpha_{\text{chlorite-water}}$ diagram (Figure 13) [65,66] were between 350 °C to 450 °C, where the chlorite-water pair fractionation yielded values from +3.17‰ at 350 °C to +4.46‰ at 400 °C, confirming the presence of a hydrothermal-meteoric fluid in equilibrium with scheelite crystallization.

The mixing of magmatic and metamorphic fluids with different origin in granite systems has been inferred in the literature, where the external fluids (i.e., metamorphic, hydrothermal-meteoric) can mix and dilute the primary magmatic fluid, even when en-

riched by metals extracted from wall-rocks in the frame of the resulting convective circulation [93–95].

5.4. Chlorite Geothermometer

Chlorite consists of a 2:1 layer with a negative charge $[(R^{2+}, R^{2+})_3(xSi_4R^{2+}_y)O_{10}OH_2]^-$ balanced by a positively charged interlayer octahedral sheet $[(R^{2+}, R^{3+})_3(OH)_6]^+$. $R^{2+,3+}$ is represented by Mg, Fe(II), and Fe(III) with Mg-rich chlorite (clinochlore) generally being metamorphic (high temperature), while the Fe-rich chlorite (chamosite) is typically diagenetic (low temperature). Additionally, Ni-rich chlorite (nimite) and Mn-rich chlorite (pennantite) are the other two less common varieties of chlorite. Most chlorites are trioctahedral in both sheets, i.e., the ferric iron content is low. Furthermore, it is well known that the ubiquitous and large thermodynamic stability of chlorite is in metamorphic, diagenetic, and hydrothermal systems, where its chemical composition is influenced by temperature and pressure. Thus, chlorite may crystallize over a large range of temperatures from 80 °C to more than 700 °C and pressures from 1 Kbar to 12 Kbar [96]. For example, cookeite, a Li-di, trioctahedral chlorite, is an example of a polymorph that has crystallized at low to high pressures [97,98].

The Fe,Mn-chlorite associated with W mineralizations from Borralha crystallized directly from the hydrothermal fluid and isotopically re-equilibrated with respect to scheelite. Hydrothermal fluids in the crust generally have a low oxidation potential and dissolved Fe predominantly occurs in its +2 oxidation state [99]. Under these reduced conditions, the amount of Fe^{3+} in hydrothermal fluids is negligible compared to that of Fe^{2+} [71]. Both Fe and Mn were available in the hydrothermal fluid from wolframite replaced by scheelite. Considering the textural relationships observed between wolframite to scheelite and Fe,Mn-chlorite, and the high amount of Fe and Mn in the hydrothermal fluid, chlorite crystallized after scheelite preserving the redox conditions during the fluid migration. The redox conditions are supported by the obtained FI data, where CO_2 and CH_4 subsequently reduced oxidation. By contrast, adequate oxidizing conditions were needed to buffer the oxygen activity in the case of a hydrothermal fluid with a Fe- or Mn-poor or -rich character and a low fluid/rock ratio. In this case, both Fe^{3+} and Mn^{3+} had a limited stability field in aqueous solution, being rapidly trapped during chlorite crystal growth.

Several authors have suggested that empirical or semi-empirical geothermometers have only been developed for the most common chlorites (i.e., Al-, Fe-, or Mg-rich chlorites) and it could worth extending to rarer chlorites, like Mn-rich chlorite [29], because the actual geothermometers do not include a Mn-rich end-member, such as pennantite. Nevertheless, the systematic presence of measurable amounts of Mn has been tested as a new pathfinder for chlorites developed in the course of ore-forming processes. A valid example is related to Fe,Mg,Mn-chlorite identified in Pb-Zn, Bi, and Ag ore veins from the Toyoha geothermal system, Japan [70]. In this case, the structural formula calculation, similar to ferric iron, will arise without the quantification of the total Mn^{3+}/Mn ratio, but the ratio of Mn^{3+}/Mn^{2+} would probably theoretically modify the chlorite's structural formula [29]. Nevertheless, the presence of Mn^{3+} in chlorite, which would eventually be substituted with Al^{3+} in the octahedral site, is expected to lead to the structural distortion of chlorite due to the different ionic radii of Al^{3+} (0.535 Å) and Mn^{3+} (0.645 Å) [100].

The chemical compositions of Fe,Mn-chlorite are plotted in the field of daphnite (average Si = 5.30 apfu and Fe 7.51 apfu) in the Si vs. Fe_{tot} diagram (not shown) or in the field of daphnite-amesite according to the Si vs. R^{2+} diagram (Figure 6; [61]), which makes it valid for the four-thermodynamic-component solid-solution model (Mg-sudoite, Mg-amesite, clinochlore, and daphnite) used for semi-empirical geothermometers.

The estimated Fe,Mn-chlorite temperatures using the semi-empirical thermometer of Lanari [59] were about 373 °C and 458 °C ($Fe_{total} = FeO$) and 435 °C and 519 °C ($Fe_{total} = FeO$) (Bourdelle [58]). This represents average values of 415 and 477 °C. If we consider the uncertainty of 50–60 °C for T °C > 300 °C suggested by Bourdelle [58], we propose a temperature between 375 °C to 410 °C. The estimated temperatures calculated from

semi-empirical thermometers seem to be supported by the $\delta^{18}\text{O}_{\text{Fluid}}$ calculated using the fractionation equation for the chlorite-water pair [53] which confirmed a temperature of chlorite crystallization estimated at around 400 °C.

The magmatic-hydrothermal vs. metamorphic fluid circulation evidences was proposed in this work based on FI data and the oxygen stable isotope fingerprints obtained on tungstates, quartz, and Fe,Mn-chlorite (Figure 14). The presence of a metamorphic fluid with an aqueous-carbonic composition and low salinity was contributed to wolframite destabilization and scheelite precipitation in the presence of Ca^{2+} derived from plagioclase alteration. During boiling, the CO_2 was removed from the aqueous-carbonic fluid, favoring W transport [84], where Fe,Mn-chlorite crystallized after scheelite crystallization at a temperature close to the crystallization of scheelite.

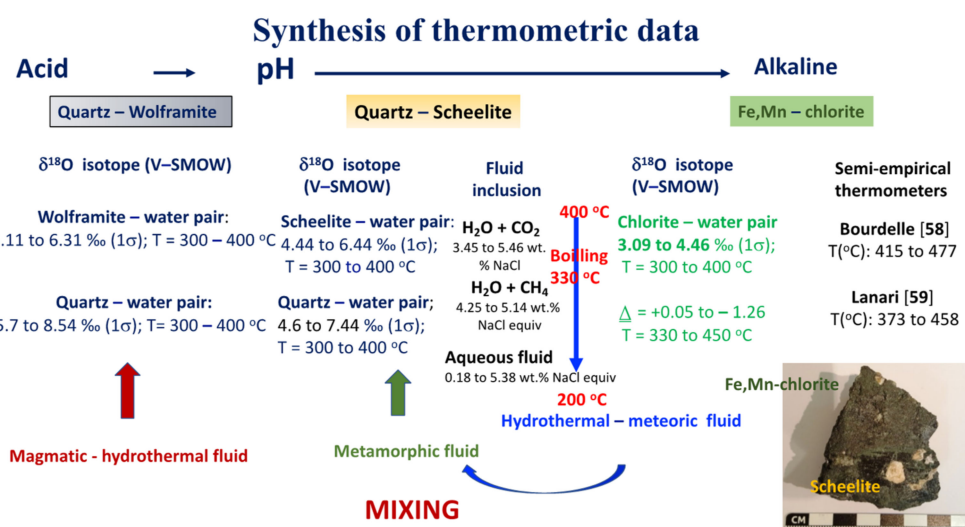


Figure 14. Synthesis of microthermometry and oxygen isotope data correlated with semi-empirical chlorite thermometers [58,59].

6. Conclusions on Fe,Mn-Chlorite Thermometry

The diversity of chlorite minerals in fossils or active hydrothermal systems is connected in most cases with the alteration types of magmatic rocks, where chlorite may crystallize directly from a solution or replace the primary minerals. The sequence of mineral pairs identified in the W, (Cu,Mo) ore deposit of Borralha satisfies all conditions to evaluate the oxygen isotope signature between tungstates and silicates. Besides, the question arises on Mn-oxidation, the effect of fluid chemistry on the mineral-water fractionation factor in chlorite may represent an uncertainty however, fractionation factors between minerals and aqueous solutions are independent of solution chemistry.

Our multiproxy study based on FIs, stable isotopes, and semi-empirical chlorite thermometers showed good consistency between the results obtained. Combining FIs and oxygen isotope geochemistry data, it was revealed that a metamorphic fluid supported the crystallization of scheelite and quartz at temperatures below 400 °C. The geothermometers applied according to Lanari and Bourdelle for Fe,Mn-chlorite produced temperature estimates between 373 °C and 458 °C, and 435 °C and 519 °C, respectively. The $\Delta_{\text{chlorite-water}}$ calculated fractionation factor corresponded to temperatures of 380 °C and 450 °C, respectively. An average chlorite crystallization temperature of 400 °C was assumed considering an uncertainty of 50–60 °C for T °C > 300 °C, as suggested by the authors of the geothermometers.

Supplementary Materials: The following are available online: <https://www.mdpi.com/article/10.3390/min12010024/s1>. Table S1. The CO_2 , CH_4 and N_2 (mol%) of aqueous-carbonic fluid measured by Raman spectroscopy analysis (50 analyses).

Author Contributions: Conceptualization, I.B., C.M.d.S. and F.N.; Formal analysis, I.B.; Investigation, I.B. and C.M.d.S.; Methodology, I.B., C.M.d.S. and F.N.; Writing—original draft, I.B. and C.M.d.S.; Writing—review and editing, I.B., C.M.d.S. and F.N. All authors have read and agreed to the published version of the manuscript.

Funding: POCTEP-ESMIMET 2018–2020 Interreg Spain-Portugal Financed by POCTEP.

Acknowledgments: This work was developed in the frame of projects POCTEP-ESMIMET 2018–2020 Interreg Spain-Portugal Financed by POCTEP and UIDB/04683/2020 ICTerra, FCT -Lisboa. Carlos Sá acknowledge the post-doc scholarship attributed in the frame of this project during 2019–2020. Thanks also to ICTerra-Polo Porto for using the fluid inclusions lab. The first author is greatly indebted to F. Nieto and Franck Bourdelle for their thorough reading and helpful suggestions carried out on an early manuscript. The authors are grateful to the Academic Editor and to all three reviewers who contributed with many suggestions and greatly improved the final manuscript version. Also thanks to Mark Ryan who reviewed the English presentation.

Conflicts of Interest: The authors declare no conflict of interest.

References

- Ren, Y.S.; Zhao, H.L.; Lei, E.; Wang, H.; Ju, N.; Wu, C.Z. Trace element and rare earth element geochemistry of the scheelite and ore genesis of the Yangjingou large scheelite deposit in Yanbian area, northeastern China, China. *Acta Petrol. Sin.* **2010**, *26*, 3720–3726.
- Song, G.; Qin, K.; Li, G.; Evans, N.G.; Chen, L. Scheelite elemental and isotopic signatures: Implications for the genesis of skarn-type W-Mo deposits in the Chizhou Area, Anhui Province, Eastern China. *Am. Miner.* **2014**, *99*, 303–317. [[CrossRef](#)]
- Poulin, R.S.; McDonald, A.M.; Kontak, D.J.; McClenaghan, M.B. On the relationship between cathodoluminescence and the chemical composition of scheelite from geologically diverse ore-deposit environments. *Can. Miner.* **2016**, *54*, 1147–1173. [[CrossRef](#)]
- Poulin, R.S.; Kontak, D.J.; McDonald, A.; McClenaghan, M.B. Assessing scheelite as an ore-deposit discriminator using its trace-element and REE chemistry. *Can. Miner.* **2018**, *56*, 265–302. [[CrossRef](#)]
- Guo, S.; Chen, Y.; Liu, C.-Z.; Wang, J.-G.; Su, B.; Gao, Y.-J.; Wu, F.-Y.; Sein, K.; Yang, Y.-H.; Mao, Q. Scheelite and coexisting F-rich zoned garnet, vesuvianite, fluorite, and apatite in calc-silicate rocks from the Mogok metamorphic belt, Myanmar: Implications for metasomatism in marble and the role of halogens in W mobilization and mineralization. *J. Asian Earth Sci.* **2016**, *117*, 82–106. [[CrossRef](#)]
- Wang, H.; Feng, C.; Zhao, Y.; Zhang, M.; Chen, R.; Chen, J. Ore genesis of the Lunwei granite-related scheelite deposit in the Wuyi Metallogenic belt, southeast China: Constraints from geochronology, fluid inclusions, and H-O-S isotopes. *Res. Geol.* **2016**, *66*, 240–258. [[CrossRef](#)]
- Wang, Y.C.; Wang, K.Y.; Konare, Y. N₂-rich fluid in the vein-type Yangjingou scheelite deposit, Yanbian, NE China. *Sci. Rep.* **2018**, *8*, 5662. [[CrossRef](#)]
- Chen, J.; Sheng, D.; Shao, Y.; Zhang, J.; Liu, Z.; Wei, H.; Yang, Q.; Luo, X.; Du, Y. Silurian S-type granite-related W-(Mo) mineralization in the Nanling Range, south China: A case study of the Pingtan W-(Mo) deposit. *Ore Geol. Rev.* **2019**, *107*, 186–200. [[CrossRef](#)]
- Kiliyas, S.P.; Konnerup-Madsen, J. Fluid inclusion and stable isotope evidence for the genesis of quartz-scheelite veins, Metagitsi area, central Chalkidiki Peninsula, N. Greece. *Miner. Depos.* **1997**, *32*, 581–595. [[CrossRef](#)]
- Sciuba, M.; Beaudoin, G.; Grzela, D.; Makvandi, S. Trace element composition of scheelite in orogenic gold deposits. *Miner. Depos.* **2019**, *55*, 1149–1172. [[CrossRef](#)]
- Meinert, L.D.; Dipple, G.M.; Nicolescu, S. World Skarn Deposits. In *Economic Geology 100th Anniversary Volume*; Hedenquist, J.W., Thompson, J.F.H., Goldfarb, R.J., Richards, J.P., Eds.; Society of Economic Geologists, Inc.: Littleton, CO, USA, 2005; pp. 299–336.
- Li, W.; Xie, G.Q.; Cook, N.J.; Mao, J.W.; Li, C.; Ciobanu, C.L.; Zhang, Z.Y. Tracking dynamic hydrothermal processes: Textures, in-situ Sr-Nd isotopes and trace element analysis of scheelite from the Yangjiashan vein-type W deposit, South China. *Am. Miner.* **2021**, *106*, 1987–2002. [[CrossRef](#)]
- Wang, G.W.; Li, R.X.; Carranza, E.J.M.; Zhang, S.T.; Yan, C.H.; Zhu, Y.Y.; Qu, J.N.; Hong, D.M.; Song, Y.W.; Han, J.W. 3D geological modeling for prediction of subsurface Mo targets in the Luanchuan district, China. *Ore Geol. Rev.* **2015**, *71*, 270–274. [[CrossRef](#)]
- McClenaghan, M.B.; Cabri, L.J. Review of gold and platinum group element (PGE) indicator minerals methods for surficial sediment sampling. *Geochem. Explor. Environ. Anal.* **2011**, *11*, 251–263. [[CrossRef](#)]
- Mishra, B.; Pruseth, K.L.; Hazarika, P.; Chinnasamy, S.S. Nature and source of the ore-forming associated with orogenic gold-deposits in the Dharwar Craton. *Geosci. Front.* **2018**, *9*, 715–726. [[CrossRef](#)]
- Singoyi, B.; Zaw, K. A petrological and fluid inclusion study of magnetite-scheelite skarn mineralization at Kara, Northwestern Tasmania: Implications for ore genesis. *Chem. Geol.* **2001**, *173*, 239–253. [[CrossRef](#)]
- Zaw, K. The CanTung E-Zone Orebody, Northwest Territories: A Major Scheelite Skarn Deposit. Unpublished Master's Thesis, Queen's University, Kingston, ON, Canada, 1976.

18. Zaw, K.; Clark, A.H. Fluoride–hydroxyl ratios of skarn silicates, CanTung E-zone scheelite orebody, Tungsten, Northwest Territories. *Can. Miner.* **1978**, *16*, 207–221.
19. Song, S.W.; Mao, J.W.; Xie, G.Q.; Jian, W.; Chen, G.H.; Rao, J.F.; Ouyang, Y.P. Petrogenesis of scheelite-bearing albitite as an indicator for the formation of a world-class scheelite skarn deposit: A case study of the Zhuxi tungsten deposit. *Econ. Geol.* **2021**, *116*, 91–121. [\[CrossRef\]](#)
20. Yuvan, J.; Shelton, K.; Falck, H. Geochemical investigations of the high-grade quartz-scheelite veins of the Cantung mine, Northwest Territories. *Geol. Surv. Can. Open File* **2007**, *5344*, 177–190.
21. Xie, G.; Mao, J.; Li, W.; Fu, B.; Zhang, Z. Granite-related Yangjiashan tungsten deposit, southern China. *Miner. Depos.* **2019**, *54*, 67–80. [\[CrossRef\]](#)
22. Wilkinson, J.J.; Zhaoshan Chang, Z.; Cooke, D.R.; Baker, M.J.; Wilkinson, C.C.; Inglis, S.; Chen, H.; Gemmell, J.B. The chlorite proximator: A new tool for detecting porphyry ore deposits. *J. Geochem. Explor.* **2015**, *152*, 10–26. [\[CrossRef\]](#)
23. Walshe, J.L. A six-component chlorite solid solution model and the conditions of chlorite formation in hydrothermal and geothermal systems. *Econ. Geol.* **1986**, *81*, 681–703. [\[CrossRef\]](#)
24. Cathelineau, M.; Nieva, D. A chlorite solid solution geothermometer the Los Azufres (Mexico) geothermal system. *Contrib. Miner. Petrol.* **1985**, *91*, 235–244. [\[CrossRef\]](#)
25. Sillitoe, R.H. Porphyry copper systems. *Econ. Geol.* **2010**, *105*, 3–41. [\[CrossRef\]](#)
26. Hsu, L.C. The stability relations of the wolframite series. *Am. Miner.* **1976**, *61*, 944–955.
27. Amossé, J. Physicochemical Study of the Hubnerite-Ferberite ($\text{MnWO}_4\text{--FeWO}_4$) zonal distribution in wolframite ($\text{Mn}_x\text{Fe}_{(1-x)}\text{WO}_4$) Deposits. Application to the Borralha Mine. *Phys. Chem. Miner.* **1978**, *3*, 331–341. (In Portuguese) [\[CrossRef\]](#)
28. Bobos, I.; Noronha, F.; Mateus, A. Fe-, Fe,Mn- and Fe,Mg-chlorite: A genetic linkage to W, (Cu,Mo)-mineralization in the magmatic-hydrothermal system of Borralha, Northern Portugal. *Miner. Mag.* **2018**, *82*, 259–279. [\[CrossRef\]](#)
29. Bourdelle, F. Low-Temperature chlorite geothermometry and related recent analytical advances: A review. *Minerals* **2021**, *11*, 130. [\[CrossRef\]](#)
30. Ribeiro, A.; Pereira, E.; Dias, R. Structure in the Iberian Peninsula. In *Pre-Mesozoic Geology of Iberia*; Dallmeyer, R.D., Martinez, G., Eds.; Springer: Berlin, Germany, 1990; pp. 220–236.
31. Ribeiro, A.; Munhá, J.; Dias, R.; Mateus, A.; Peirera, E.; Ribeiro, L.; Fonseca, P.; Araújo, A.; Oliveira, T.; Romão, J.; et al. Geodynamic evolution of the SW Europe Variscides. *Tectonics* **2007**, *26*, 1–24. [\[CrossRef\]](#)
32. Matte, P. Accretionary history and crustal evolution of the Variscan Belt in Western Europe. *Tectonophysics* **1991**, *196*, 309–337. [\[CrossRef\]](#)
33. Ribeiro, A. Contribution à l'étude tectonique de Trás-os-Montes Oriental. *Comunic. Serv. Geológicos Port.* **1974**, *24*, 1–168.
34. Noronha, F.; Ramos, J.M.F.; Rebelo, J.; Ribeiro, A.; Ribeiro, M.L. Essai de corrélation des phases de déformation hercyniennes dans le NW de la Péninsule Ibérique. *Leidsche Geol. Meded.* **1981**, *52*, 89–91.
35. Ferreira, N.; Iglesias, M.; Noronha, F.; Pereira, E.; Ribeiro, A.; Ribeiro, M.L. Granitoides da Zona Centro Ibérica e seu enquadramento geodinâmico. In *Geologia de Los Granitoides y Rocas Asociadas del Macizo Hesperico*; Bea, F., Carnicero, A., Gonzalo, J., Lopez Plaza, M., Rodriguez Alonso, M., Eds.; Libro de Homenaje a García de Figuerola L.C.; Rueda: Madrid, Spain, 1987; pp. 37–51.
36. Dias, R.; Ribeiro, A. The Ibero-Armorican Arc: A collision effect against an irregular continent? *Tectonophysics* **1995**, *246*, 113–128. [\[CrossRef\]](#)
37. Noronha, F. Les brèches du gisement de tungstène de Borralha (Nord du Portugal). Quelques données pour leur classification. *Public. Domus. Laboratório Mineral. Geológico Fac. Ciências Porto* **1979**, *4*, 187–212.
38. Noronha, F. Caractéristiques physico-chimiques des fluides associés à la genèse du gisement de tungsten de Borralha (Nord Portugal). *Bull. Miner.* **1984**, *107*, 273–284. [\[CrossRef\]](#)
39. Noronha, F.; Vindel, E.; López, J.A.; Dória, A.; García, E.; Boiron, M.C.; Cathelineau, M. Fluids related to tungsten ore deposits in Northern Portugal and Spanish Central system: A comparative study. *Rev. Soc. Geol. España* **1999**, *12*, 397–403.
40. Noronha, F. Metallogenic Study of the Wore Deposit of Borralha. Ph.D. Thesis, Universidade do Porto, Porto, Portugal, 1983. Unpublished work (In Portuguese).
41. Roedder, E. Fluid inclusions. *Rev. Miner. Geochem.* **1984**, *12*, 644.
42. Van den Kerkhof, A.M.; Hein, U.F. Fluid Inclusion Petrography. *Lithos* **2001**, *55*, 27–47. [\[CrossRef\]](#)
43. Shepherd, T.J.; Rankin, A.H.; Alderton, D.H.M. *A Practical Guide to Fluid Inclusion Studies*; Blackie & Son Ltd.: Glasgow, UK, 1985; 239p.
44. Poty, B.; Leroy, J.; Jachimowicz, L. Un nouvel appareil pour la mesure des températures sous le microscope: I: Installation de microthermometrie Chaixmeca. *Bull. Miner.* **1976**, *99*, 182–186.
45. Bakker, R.J. Package FLUIDS Computer programs for analysis of fluid inclusion data and modeling bulk fluid properties. *Chem. Geol.* **2003**, *194*, 3–23. [\[CrossRef\]](#)
46. Touret, J. The significance of fluid inclusions in metamorphic rocks. In *Thermodynamics in Geology*; Fraser, D.G., Ed.; Amsterdam Reidel Pub. Co.: Dordrecht, The Netherlands, 1977; pp. 203–227.
47. Ramboz, C.; Schnapper, D.; Dubessy, J. The P-V-T-X- FO_2 evolution of $\text{H}_2\text{O--CO}_2\text{--CH}_4$ bearing fluid in a wolframite vein: Reconstruction from fluid inclusion studies. *Geochim. Cosmochim. Acta* **1985**, *49*, 205–219. [\[CrossRef\]](#)
48. Prieto, A.C.; Guedes, A.; Doria, A.; Noronha, F.; Jimenez, J. Quantitative determination of gaseous phases in fluid inclusions by Raman microspectrometry. *Spectr. Lett.* **2012**, *45*, 1–5. [\[CrossRef\]](#)

49. Clayton, R.N.; Mayeda, T.K. The use of bromide pentafluoride in the extraction of oxygen from oxides and silicates for isotopic analysis. *Geochim. Cosmochim. Acta* **1963**, *27*, 43–52. [\[CrossRef\]](#)
50. Zhang, L.; Liu, J.; Zhou, H.; Chen, Z. Oxygen isotope fractionation in the quartz-water-salt system. *Econ. Geol.* **1989**, *84*, 1643–1650. [\[CrossRef\]](#)
51. Landis, G.P.; Rye, R.O. Geologic, fluid inclusion, and stable isotope studies of the Pasto Bueno tungsten-base metal ore deposit northern Peru. *Econ. Geol.* **1974**, *69*, 1025–1059. [\[CrossRef\]](#)
52. Wesolowski, D.; Ohmoto, H. Calculated oxygen isotope fractionation factors between water and the minerals scheelite and powellite. *Econ. Geol.* **1986**, *81*, 471–477. [\[CrossRef\]](#)
53. Wenner, D.B.; Taylor, H.R., Jr. Temperatures of serpentinization of ultramafic rocks based on $^{18}\text{O}/^{16}\text{O}$ fractionation between coexisting serpentine and magnetite. *Contrib. Miner. Petrol.* **1971**, *32*, 165–168. [\[CrossRef\]](#)
54. Clayton, R.N.; O'Neil, J.R.; Mayeda, T.K. Oxygen isotope exchange between quartz and water. *Geophys. Res.* **1972**, *77*, 3057–3067. [\[CrossRef\]](#)
55. Brugger, J.; Gieré, R.; Grobe, B.; Uspenski, E. Scheelite -powellite and paraniite-(Y) from the Fe-Mn deposit at Fianel, Eastern Swiss Alps. *Am. Miner.* **1998**, *83*, 1100–1110. [\[CrossRef\]](#)
56. Bailey, S.W. Clinochlores: Structures and crystal chemistry, In: *Hydrous Phyllosilicates* (S.W. Bailey, editor), Mineralogical Society of America, Washington. *Rev. Miner.* **1988**, *19*, 398–404.
57. Nieto, F. Chemical composition of metapelitic chlorites: X-ray diffraction and optical property approach. *Eur. J. Miner.* **1997**, *9*, 829–841. [\[CrossRef\]](#)
58. Bourdelle, F.; Parra, T.; Chopin, C.; Beyssac, O. A new chlorite geothermometer for diagenetic to low-grade metamorphic conditions. *Contrib. Miner. Petrol.* **2013**, *165*, 723–735. [\[CrossRef\]](#)
59. Lanari, P.; Wagner, T.; Vidal, O. A thermodynamic model for di-trioctahedral chlorite from experimental and natural data in the system $\text{MgO-FeO-Al}_2\text{O}_3\text{-SiO}_3\text{-H}_2\text{O}$: Applications to P-T sections and geothermometry. *Contrib. Miner. Petrol.* **2014**, *167*, 968–984. [\[CrossRef\]](#)
60. Inoue, A.; Meunier, A.; Patrier-Mas, P.; Rigault, C.; Beaufort, D.; Vieillard, P. Application of chemical geothermometry to low-temperature trioctahedral chlorites. *Clays Clay Miner.* **2009**, *57*, 371–382. [\[CrossRef\]](#)
61. Wiewióra, A.; Weiss, Z. Crystallochemical classifications of phyllosilicates based on the unified system of projection of chemical composition: II. The chlorite group. *Clay Miner.* **1990**, *25*, 83–92. [\[CrossRef\]](#)
62. Jacobson, C.E. Estimation of Fe^{3+} from electron microprobe analyses: Observations on calcic amphibole and chlorite. *J. Metamorf. Geol.* **1989**, *7*, 507–513. [\[CrossRef\]](#)
63. Shieh, Y.N.; Zhang, G.X. Stable isotope studies of quartz-vein type tungsten deposits in Dajistan mine, Jiangxi Province, Southeast China. In *Stable Isotope Geochemistry: A Tribute to Samuel Epstein*; Taylor, H.P., O'Neil, J.R., Kaplan, I.R., Eds.; SPE Publ.: London, UK, 1991; Volume 3, pp. 425–435.
64. Zheng, Y.-F. Oxygen isotope fractionation in wolframite. *Eur. J. Miner.* **1992**, *4*, 1133–1135. [\[CrossRef\]](#)
65. Wenner, D.B.; Taylor, H.P., Jr. Oxygen and hydrogen isotope studies of the serpentinization of ultramafic rocks in oceanic environments and continental complexes. *Am. J. Sci.* **1973**, *273*, 207–239. [\[CrossRef\]](#)
66. Cole, D.R. A preliminary evaluation of oxygen isotopic exchange between chlorite-water. *Geol. Soc. Am. Annu. Meet.* **1985**, *17*, 550.
67. Cathelineau, M. Cation site occupancy in chlorites and illites as a function of temperature. *Clay Miner.* **1988**, *23*, 471–485. [\[CrossRef\]](#)
68. Jowett, E.C. Fitting Iron and Magnesium into the Hydrothermal Chlorite Geothermometer. In *Proceedings of the GAC/MAC/SEG Joint Annual Meeting*, Toronto, ON, Canada, 27–29 May 1991.
69. Bourdelle, F.; Cathelineau, M. Low-temperature chlorite geothermometry: A graphical representation based on a $\text{T-R}^{2+}\text{-Si}$ diagram. *Eur. J. Miner.* **2015**, *27*, 617–626. [\[CrossRef\]](#)
70. Inoue, A.; Kurokawa, K.; Hatta, T. Application of chlorite geothermometry to hydrothermal alteration in Toyoha geothermal system, southwestern Hokkaido, Japan. *Res. Geol.* **2010**, *60*, 52–70. [\[CrossRef\]](#)
71. Inoue, A.; Inoue, S.; Utada, M. Application of chlorite thermometry to estimation of formation temperature and redox conditions. *Clay Miner.* **2018**, *53*, 143–158. [\[CrossRef\]](#)
72. Verdecchia, S.O.; Collo, G.; Zandomeni, P.S.; Wunderlin, C.; Fernhrmann, M. Crystallochemical index and geothermobarometric calculations as a multiproxy approach to P-T condition of the low-grade metamorphism: The case of the San Luis Formation, eastern Sierras Pampeanas. *Lithos* **2019**, *324–325*, 385–401. [\[CrossRef\]](#)
73. Wood, S.A.; Samson, I.M. The hydrothermal geochemistry of tungsten in granitoid environments: I. Relative solubilities of ferberite and scheelite as a function of T, P, pH and m_{HCl} . *Econ. Geol.* **2000**, *95*, 143–182. [\[CrossRef\]](#)
74. Oelsner, O. Über Erzgebirgische Wolframite. *Ber. Freib. Geol. Ges.* **1944**, *20*, 44–49.
75. Leutwein, F. Die chemische Zusammensetzung der Wolframite und ihre lagerstättenkundliche Bedeutung. *Acta Geol. Akad. Sci. Hungary* **1952**, *1*, 133–141.
76. Taylor, R.G.; Hosking, K.F.G. Manganese-iron ratios in wolframites, South Crofty Mine, Cornwall. *Econ. Geol.* **1970**, *65*, 47–53. [\[CrossRef\]](#)
77. Moore, F.; Howie, R.A. On the application of the hubnerite ferberite ratio as a Geothermometer. *Miner. Depos.* **1978**, *13*, 391–397. [\[CrossRef\]](#)

78. Michaud, J.A.; Pichavant, M. The H/F ratio as an indicator of contrasted wolframite deposition mechanisms. *Ore Geol. Rev.* **2019**, *104*, 266–272. [[CrossRef](#)]
79. Lecumberri-Sanchez, P.; Vieira, R.; Heinrich, C.A.; Pinto, F.; Wälle, M. Fluid-rock interaction is decisive for the formation of tungsten deposits. *Geology* **2017**, *45*, 579–582. [[CrossRef](#)]
80. Baumer, A.; Caruba, R.; Guy, B. Experimental study of hydrothermal transformation scheelite in ferberite: Preliminary results. *Bull. Miner.* **1985**, *108*, 15–20. [[CrossRef](#)]
81. Reed, M.H.; Spycher, N. Calculation of high temperature pH and mineral equilibria in hydrothermal waters, with application to geothermometry and studies of boiling and dilution. *Geochim. Cosmochim. Acta* **1984**, *48*, 1479–1492. [[CrossRef](#)]
82. Reed, M.H.; Spycher, N. Boiling, cooling, and oxidation in epithermal systems: A numerical modeling approach. In *Geology and Geochemistry of Epithermal Systems*; Berger, B.R., Bethke, P.M., Eds.; Soc. Econ. Geologists: Littleton, CO, USA, 1985; Volume 2, pp. 249–272.
83. Drummond, S.E.; Ohmoto, H. Chemical evolution and mineral deposition in boiling hydrothermal systems. *Econ. Geol.* **1985**, *80*, 126–147. [[CrossRef](#)]
84. Wood, S.A.; Samson, I.M. Solubility of ore minerals and complexation of ore metals in hydrothermal solutions. *Rev. Econ. Geol.* **1998**, *10*, 33–80.
85. Phillips, G.N.; Evans, K.A. Role of CO₂ in the formation of gold deposits. *Nature* **2004**, *429*, 860–863. [[CrossRef](#)] [[PubMed](#)]
86. Higgins, N.C. Fluid inclusion evidence for the transport of tungsten by carbonate complexes in hydrothermal solutions. *Can. J. Earth Sci.* **1980**, *17*, 823–830. [[CrossRef](#)]
87. Kreulen, R.; Schuiling, R.D. N₂-CH₄-CO₂ during formation of the Dome de l'Agoul, France. *Geochim. Cosmochim. Acta* **1981**, *46*, 193–203. [[CrossRef](#)]
88. Taylor, H.P., Jr. The application of oxygen and hydrogen isotope studies to problems of hydrothermal alteration and ore deposition. *Econ. Geol.* **1974**, *69*, 843–883. [[CrossRef](#)]
89. Taylor, H.P., Jr. Oxygen and hydrogen isotope relationships in hydrothermal mineral deposits. In *Geochemistry of Hydrothermal Ore Deposits*, 2nd ed.; Barnes, H.L., Ed.; Wiley: New York, NY, USA, 1979; pp. 236–277.
90. Ohmoto, H. Stable isotope geochemistry of ore deposits. In *Stable Isotopes in High Temperature Geological Processes*; Valley, J.W., Taylor, H.P., Jr., O'Neil, J.R., Eds.; Mineralogical Society of America: Chantilly, VA, USA, 1986; Volume 16, pp. 491–559.
91. Sheppard, S.M.F. Characterization and isotopic variations in natural water. In *Stable Isotopes in High Temperature Geological Processes*; Valley, J.W., Taylor, H.P., Jr., O'Neil, J.R., Eds.; De Gruyter: Berlin, Germany, 1986; Volume 16, pp. 165–183.
92. Taylor, H.P., Jr. Oxygen and hydrogen isotope relationships in hydrothermal mineral deposits. In *Geochemistry of Hydrothermal Ore Deposits*, 3rd ed.; Barnes, H.L., Ed.; John Wiley & Sons: New York, NY, USA, 1997; pp. 229–302.
93. Marignac, C.; Cathelineau, M. *The Nature Ore-Forming Fluids in Peri-Batholithic Sn-W Deposits*; James Cook University: Townsville, Australia, 2018.
94. Polya, D.A.; Foxford, K.A.; Stuart, F.; Boyce, A.; Fallick, A.E. Evolution and paragenetic content of low D hydrothermal fluids from Panasqueira W-Sn deposit, Portugal: New evidence from microthermometric, stable isotope, noble gas and halogen analyses of primary fluid inclusions. *Geochim. Cosmochim. Acta* **2000**, *64*, 3357–3371. [[CrossRef](#)]
95. Wilkinson, J.J. The role of metamorphic fluids in the development of the Cornubian prefield: Fluid inclusion evidence from south Cornwall. *Miner. Mag.* **1990**, *54*, 219–230. [[CrossRef](#)]
96. Vidal, O.; Goffé, B. Cookeite experimental study and thermodynamic analysis of its compatibility relations in the Li₂O-Al₂O₃-SiO₂-H₂O system. *Contrib. Miner. Petrol.* **1991**, *108*, 72–81. [[CrossRef](#)]
97. Bobos, I.; Vieillard, P.; Charoy, B.; Noronha, F. Alteration of spodumene to cookeite and its thermodynamic stability. *Clays Clay Miner.* **2007**, *57*, 296–304.
98. Goffé, B.; Azanón, J.M.; Bouybaouene, M.L.; Jullien, M. Metamorphic cookeite in Alpine metapelites from the Rif (Morocco) and Betic chain (Spain). *Eur. J. Miner.* **1996**, *8*, 335–348. [[CrossRef](#)]
99. Heinrich, C.A.; Seward, T.M. A spectrophotometric study of aqueous iron (II) chloride complexing from 25 to 200 °C. *Geochim. Cosmochim. Acta* **1990**, *54*, 2207–2221. [[CrossRef](#)]
100. Burns, R.G. *Mineralogical Applications of Crystal Field Theory*; Cambridge University Press: New York, NY, USA, 1993.